Available online at www.sciencedirect.com

ScienceDirect

Advances in Space Research 72 (2023) 5047–5069

ADVANCES IN SPACE RESEARCH (a COSPAR publication)

www.elsevier.com/locate/asr

A generic three-dimensional model for solar energy reflected from mirrors in circular orbits

Onur Çelik *, Colin R. McInnes

James Watt School of Engineering, University of Glasgow, Glasgow G12 8QQ, Scotland, United Kingdom

Received 4 July 2023; received in revised form 24 August 2023; accepted 20 September 2023
Available online 26 September 2023

Abstract

Orbiting solar reflectors may be a useful assets to illuminate solar power farms to enhance their utility when direct sunlight is not available. The assessment of their feasibility for a variety of applications requires accurate calculations of how much solar energy can be delivered from a variety of orbits. This paper presents a generic, three-dimensional semi-analytical model that outputs the quantity of solar energy for a given circular orbit and solar power farm position at the beginning of a pass. The model extends previous studies by including new phenomena such as the Earth's oblateness, rotation, shadow on the reflector and orbit around the Sun, in addition to time-dependent geometric and atmospheric losses. These additions provide new analytical insights into the delivery of reflected solar energy delivery and demonstrate the importance of high-fidelity modelling. The strengths of the model are illustrated for a 1000 km altitude Sun-synchronous orbit throughout, as well as a range of other orbits and solar power farms located at different latitudes and longitudes.

Keywords: Space-based solar energy; Orbiting solar reflectors; Mathematical modelling

1. Introduction

Ultra-lightweight, large and flat orbiting solar reflectors (OSR) can be used to reflect sunlight from space onto the surface of the Earth and other planetary bodies. They were considered a useful asset even before the modern space era for the primary use of night-time illumination (Oberth, 1929). Later studies have considered the concept of OSR to enhance the utility of solar power farms beyond the hours of sunlight, agricultural production, street illumination and other climate applications (Buckingham and Watson, 1968; Billman et al., 1977; Ehricke, 1979; Canady and Allen, 1982). Unlike other space-based wireless power transmission concepts, such as solar power satellites, OSRs are decoupled from terrestrial infrastructure and can service terrestrial solar power plants, as long as it is visible to them (Çelik et al., 2022), providing a truly global space-based clean energy service. Reflectors in near-polar orbits can service solar power plants anywhere on the Earth near the dawn and dusk hours, where energy demand is high, but solar energy supply is low, due to the low (or below the horizon) elevation of the Sun. To that end, Fraas et al. proposed the employment of a 10 km reflector structure in a Sun-synchronous orbit of 1000 km altitude to deliver solar energy to 40 solar power farms across the Earth (Fraas, 2012; Fraas et al., 2013). A more recent, detailed reference architecture study of orbiting solar reflectors proposed solar energy delivery to 13 existing and proposed large solar power plants around the Earth, from a repeating ground track Sun-synchronous orbit at 884.6 km altitude (Viale et al., 2023). OSRs in polar orbits, displaced by solar radiation pressure in the anti-sunline direction can enhance the energy delivery

* Corresponding author.
E-mail addresses: Onur.Celik@glasgow.ac.uk (O. Çelik), Colin.McInnes@glasgow.ac.uk (C.R. McInnes).

https://doi.org/10.1016/j.asr.2023.09.046
0273-1177/

Nomenclature

A	area, km^2
a	semi-major axis of solar image, km
b	semi-minor axis of solar image, km
c	empirical parameter
D	diameter, km
d	slant range, km
e	eccentricity, unitless
E	energy, GWh
f	function
f	true anomaly, rad
h	altitude, km
i	orbit inclination, rad
I	solar constant, GW/km^2
J_2	second-degree zonal harmonics, unitless
k	empirical parameter
M	matrix
P	power, GW
R	radius, km
r	radius, km
T	orbit period, sec
t	time, sec
x, y, z	cartesian coordinates
$\mathbf{X}$	state
α	angle subtended by the Sun, rad
β	half of central angle, rad
γ	polar angle, rad
ϵ	elevation angle, rad
δ	auxiliary parameter for eclipse detection
η	integer, unitless
κ	scaling coefficient
λ	longitude, rad
μ	gravitational parameter, km^3/s^2
ν	generic angle, rad
ω	argument of periapsis, rad
ω	angular rate, rad/s
Ω	right ascension of the ascending node, rad
ψ	angle between incoming and outgoing sunlight, rad
ϕ	latitude, rad
ρ	distance, km
σ	power density, GW/km^2
τ	atmospheric transmission efficiency, unitless
θ	argument of latitude, rotation angle, rad
ξ	Earth's obliquity, rad

Subscripts

0	beginning; first
a	semimajor axis
b	semiminor axis
ecl	eclipse
eff	effective
E	Earth
ECI	Earth-centered inertial
ECR	Earth-centered rotating
ENU	East-North-Up frame
enu	east-north-up frame
f	end; last
gt	ground target; solar power farm
i	inertial frame
im	solar image
J_2	second-degree zonal harmonics
ORB	orbit frame
o	orbit frame; initial
p	penumbra
$pass$	orbital pass
pr	projected
r	rotating frame
ref	reflector
sta	stationary
sun	Sun
u	umbra
$\odot$	Sun

around dawn/dusk hours or extend it further into the night (Çelik and McInnes, 2022). Other recent proposals include a two-reflector constellation in anti-heliotropic orbits and polar and Sun-synchronous orbits to deliver solar energy to existing and hypothetical solar power farms (Bonetti and McInnes, 2019; Çelik and McInnes, 2023). OSRs can also be employed for lunar, Mars, and other non-terrestrial applications (Bewick et al., 2011; Çelik and McInnes, 2022). A detailed literature study is presented in Çelik et al. (2022) and a technology demonstration roadmap is discussed in Viale et al. (2022).

For OSR applications, accurate modelling of the quantity of energy delivered is of paramount importance to assess the feasibility of the concept. The geometry of the reflected solar image and atmospheric losses are a function of the elevation of the OSR from the solar power farm, which is moving with the Earth. Considering the finite size of a solar power farm, the solar image illuminates a variable area of the farm itself. The quantity of energy delivered is obtained from the integration of this effective area that captures the reflected sunlight. Yet, earlier studies largely ignored these issues and relied on simplified algebraic expressions to calculate the quantity of energy delivered. For example, geometric losses are ignored in Canady and Allen (1982), and atmospheric losses are only considered as fixed coefficients. Fraas (2012) and Fraas et al. (2013)

did attempt to include geometric and atmospheric losses, but they also considered a single fixed coefficient for both. Bonetti and McInnes (2019) considered time-variable losses, but used a numerical solution and did not provide analytical insights into the problem.

In a more recent study, Çelik and McInnes (2022) provided detailed analytical insights for the energy delivery process from polar orbit with overhead passes, including geometric losses, time-dependent atmospheric losses, and panel tilt, and presented the power profile together with non-terrestrial applications. Indeed, Çelik and McInnes (2022) used scalar modelling, resulting in an analytical solution with elliptical functions when atmospheric losses are not included. However, none of the above studies presented a (semi-)analytical formulation that includes the Earth's rotation, oblateness, shadow on the reflector and orbit around the Sun while it is valid for a range of orbits. Such an approach would make the model non-scalar, but vectorial descriptions would also extend the model applicability to orbits with a range of inclinations, to passes that are not just overhead, and to include eclipses by the Earth and the seasonal variations, increasing its fidelity. Further implications of this generic model are that the pass duration will not be fixed anymore, it will be dependent on the relative positions of the reflector and the solar power farm for a given orbit. The variable pass duration will have an impact on the energy delivered during a pass. Non-overhead or 'offset' passes will change the energy delivered as compared to overhead passes, impacting the discussion on reflector scheduling and economic breakeven.

Therefore this paper presents a generic semi-analytical model for reflected solar energy delivery from circular orbits. The aim of the model is to output the quantity of solar energy delivered for a given set of orbital elements of the orbit and the initial solar power farm position in latitude and longitude. The reflector is assumed flat and the solar power farm is assumed a circular disk. The orbit is propagated analytically and low-order variations in the orbital elements due to the Earth's oblateness are included. While the Earth is assumed oblate dynamically, it is assumed spherical for the energy delivery process, but its rotation is included in the model. Two different semi-analytical approaches are presented for calculating pass duration in the presence of the Earth's rotation and eclipses. The geometrical relationships and atmospheric losses that are previously presented in Çelik and McInnes (2022) are also included in the enhanced model and summarised in the paper. Various test cases are presented, both standalone and in comparison with previous studies to both validate it and demonstrate its strengths.

The paper is structured as follows: In the next section, the reference frames and orbital dynamics of the problem are presented. In Section 3, the geometry of the solar image is presented. The model is introduced and its details are discussed in Section 4. The model applications are discussed in Section 5 and finally, conclusions are presented in Section 6.

2. Preliminaries

2.1. Reference frames

The model of reflected solar energy delivery is such that for a given set of orbital parameters in terms of Keplerian elements and a given initial position of the solar power farm, the output is the energy delivered to the solar power farm during an orbital pass. The problem at hand then includes both the orbit and ground segments and the rotation of the Earth. Therefore, multiple reference frames will be used to describe the reflector position with respect to each. The following reference frames are considered (also shown in Fig. 1):

- *Earth-centered inertial (ECI)*: This is an equatorial reference frame whose origin is centred at the centre of the Earth, with the x-axis ($\hat{\mathbf{x}}_i$) pointing to the vernal equinox direction, and the z-axis ($\hat{\mathbf{z}}_i$) pointing to the Earth's rotation axis, and the y-axis ($\hat{\mathbf{y}}_i$) completing the triad.
- *Perifocal frame* (or *orbit frame)*: This is the reference frame in which the orbit is propagated initially. Its origin is centred at the orbit's focal point and xy-plane defines the orbit plane. The x-axis points towards the periapsis, and the z axis points towards the orbit angular momentum vector and the y-axis completes the triad. For a circular orbit considered in this paper, the position of the reflector in this frame can be described as:

$$\mathbf{X}_{ORB} = (R_E + h)\begin{bmatrix}\cos\theta\\ \sin\theta\\ 0\end{bmatrix} \tag{1}$$

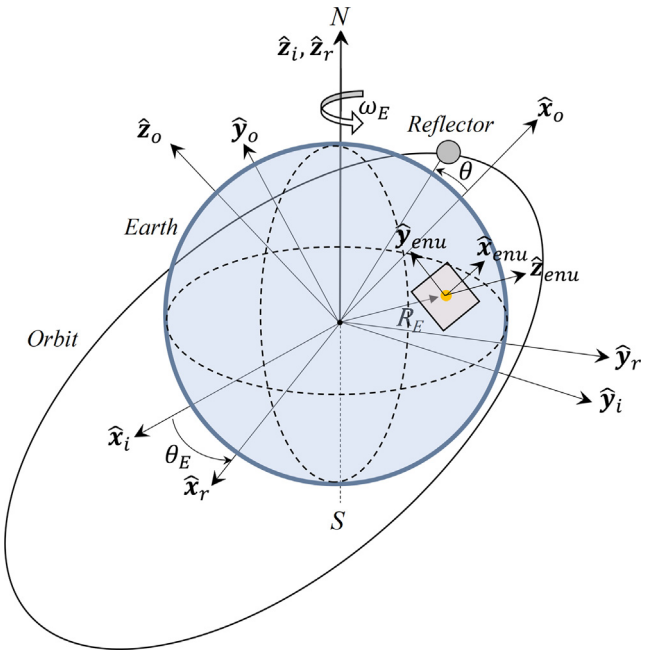

Fig. 1. Reference frames used in this paper.

where R_E is the Earth's radius ($R_E = 6378.2$ km) and h is the orbit altitude. The position in perifocal frame can be projected into the ECI frame by a 3–1-3 rotation sequence (see Appendix A for details on the rotation matrices and sequences):

$$\mathbf{X}_{ECI} = M_3(\omega)M_1(i)M_3(\Omega)\mathbf{X}_{ORB} \tag{2}$$

where ω is the argument of periapsis, i is the orbit inclination and Ω is the right ascension of the ascending node. The argument of periapsis is not defined for circular orbits, and it is assumed as 0, which results in $M_3(\omega)$ being an identity matrix.

- *Earth-centered co-rotating (ECR) frame*: The ECR frame is essentially the same reference frame as the ECI frame but it rotates around the z-axis with a rate equal to the Earth's rotation rate, $\omega_E = 7.27 \times 10^{-5}$ rad s^{-1}. The reflector position in the ECR frame can therefore be expressed by a rotation around the z-axis, such that

$$\mathbf{X}_{ECR} = M_3(\theta_E)\mathbf{X}_{ECI} \tag{3}$$

where θ_E describes the Earth's time dependent rotation, i.e., $\theta_E = \theta_{E,0} + \omega_E t$ with $\theta_{E,0}$ is the initial angular position of the ECR frame with respect to the ECI frame.

- *East-North-Up (ENU)* (or *Topocentric horizon frame*): The origin of this frame is centred at the geographical coordinates of the solar power farm (with a spherical Earth assumption) with latitude ϕ and longitude λ. The z-axis ($\hat{\mathbf{z}}_{enu}$) is parallel to the local Earth radius vector and normal to the local horizontal plane of the solar power farm. The x-axis ($\hat{\mathbf{x}}_{enu}$) or the east direction is defined as $\hat{\mathbf{x}}_{enu} = \frac{\hat{\mathbf{z}}_{enu}\times\hat{\mathbf{z}}_I}{|\hat{\mathbf{z}}_{enu}\times\hat{\mathbf{z}}_I|}$, with the y-axis completing the triad in the north direction. The position in the ECI frame can then be projected in the topocentric horizon frame by a transformation matrix such that (Curtis, 2013):

$$\mathbf{X}_{ENU} = M_{ECI}^{ENU}\mathbf{X}_{ECI} = \begin{bmatrix} -\sin\lambda & \cos\lambda & 0 \\ -\sin\phi\cos\lambda & -\sin\phi\sin\lambda & \cos\phi \\ \cos\phi\cos\lambda & \cos\phi\sin\lambda & \sin\phi \end{bmatrix}\mathbf{X}_{ECI} \tag{4}$$

This expression provides the position of the reflector in ENU for an instantaneous longitude. However, the Earth's rotation means that λ will also vary by the same rate, and the position in each instant of a pass can be described in the instantaneous ENU frame as:

$$\mathbf{X}_{ENU} = M_{ECI}^{ENU}M_3(\theta_E)\mathbf{X}_{ECI} = M_{ECI}^{ENU}\mathbf{X}_{ECR} \tag{5}$$

Finally, in order to describe the position relative to the Earth's surface, a translation by the Earth's radius needs to be performed along the $\hat{\mathbf{z}}_{enu}$ axis, such that:

$$\mathbf{X}_{ENU} = M_{ECI}^{ENU}\mathbf{X}_{ECR} = M_{ECI}^{ENU}M_3(\theta_E)\mathbf{X}_{ECI} - [0,0,R_E]^T \tag{6}$$

In the implementation of the model, the orbit is first propagated in the perifocal frame, then it is projected onto the topocentric frame, following a sequence of transformations from perifocal to the ECI frame and from the ECI frame to the ECR frame. Although each is described separately, the transformations are often not performed collectively in a single step, similar to Eq. (6). This will also be seen in the analytical slant range expression in the following sections. Before discussing these issues the orbital dynamics aspects of the problem will be presented in the next subsection.

2.2. Orbit dynamics

A circular orbit is considered at altitude h and radius $R_E + h$, inclination i, right ascension of the ascending node Ω and argument of latitude θ, which can be expressed as $\theta = \omega + f$, where ω denotes argument of periapsis and f denotes true anomaly. ω is not defined for circular orbits and f is set to zero at the beginning of the simulations. The position of the solar reflector in the perifocal frame is given in Eq. (1), in which, the argument of latitude, θ, is propagated as follows:

$$\theta = \theta_o + \omega_o t \tag{7}$$

where θ_o is the initial argument of latitude and ω_o is the mean motion, which is found from:

$$\omega_o = \frac{2\pi}{T} = \frac{2\pi}{2\pi\sqrt{\frac{(R_E+h)^3}{\mu}}} = \sqrt{\frac{\mu}{(R_E+h)^3}} \tag{8}$$

where T is the orbit period and μ denotes the gravitational parameter equal to 398600 km^3 s^{-2} (Chobotov, 2002). However, the effect of the Earth's oblateness will also perturb the orbit period. In this paper, the Earth's oblateness up to the second degree zonal harmonics (i.e., $J_2 = 1.08263 \times 10^{-3}$ (Chobotov, 2002)) is implemented. The variation of the orbit period as a result of the J_2 effect is given as (Chobotov, 2002):

$$T_{J_2} = T\left[1 - \frac{3}{2}J_2\frac{R_E^2}{(R_E+h)^2} - \frac{3}{4}J_2\frac{(4-5\sin^2 i)R_E^2}{(R_E+h)^2}\right] \tag{9}$$

The J_2-corrected mean motion will then be:

$$\omega_{o,J_2} = \frac{2\pi}{T_{J_2}} \tag{10}$$

The Earth's oblateness also causes variations in Ω and ω. Even though the latter is undefined for a circular orbit, the effect of the Earth's oblateness still results in an angular shift in the start/end point of the orbit due to orbit rotation. The time rate of change of Ω and ω induced by the Earth's oblateness can be expressed for circular orbits as (Chobotov, 2002):

$$\dot{\Omega} = -\frac{3}{2}J_2\left[\frac{\sqrt{\mu}R_E^2}{(R_E+h)^{7/2}}\right]\cos i \tag{11}$$

$$\dot{\omega} = -\frac{3}{2}J_2\left[\frac{\sqrt{\mu}R_E^2}{(R_E+h)^{7/2}}\right]\left(\frac{5}{2}\sin^2 i - 2\right) \tag{12}$$

Then, the linear change in Ω and ω as the orbit propagates will be:

$$\Omega = \Omega_0 + \dot{\Omega} t \tag{13}$$

$$\omega = \omega_0 + \dot{\omega} t \tag{14}$$

where Ω_0 denotes the initial values of the right ascension of the ascending node and the argument of periapsis. These relationships are used when propagating the orbit and calculating the slant range. It is worth noting that the Earth's oblateness also causes variations in other orbital elements, but they are generally negligible for circular orbits over an orbit period (Chobotov, 2002), and therefore are not included in this study. They can be more influential when the orbits are elliptical, which will be discussed later. In the next section, the relationships derived in this and the previous sections will be used to define the projected image of the solar disk.

3. Geometry of the solar image

An image of the solar disk is projected onto a solar power farm as soon as the reflector rises in the local horizontal plane of the solar power farm until the reflector sets again at the local horizontal plane, as shown in Fig. 2. This image is elliptical and its time-dependent size is a function of the slant range, elevation from the local horizon, and the angle subtended by the Sun, as shown in Fig. 3 and expressed below (Canady and Allen, 1982), such that:

$$b(t) = d(t)\tan(\alpha/2) \tag{15a}$$

$$a(t) = \frac{b(t)}{\sin\epsilon(t)} \tag{15b}$$

where $a(t)$ and $b(t)$ denote semi-major and semi-minor axis of the projected solar image. Then, $d(t), \epsilon(t)$ and α are the slant range, the elevation of the reflector from the local horizon and the angle subtended by the Sun. Even before any analysis, it can be stated that the solar image will be stretched to infinity in its semi-major axis at the instant that the reflector rises and sets at the local horizon. If the maximum elevation reaches 90 deg, i.e., a direct overhead pass, then the solar image will be circular. But it will be shown later that in most cases the maximum elevation will be less than 90 deg due to the Earth's rotation.

The slant range is the first parameter to be investigated. It is defined as the distance from the solar power farm point and is expressed in the topocentric horizon frame. Considering the rotating Earth and an orbit propagated in the orbit frame, the position of the reflector can be expressed in the topocentric coordinate frame, $\mathbf{X}_{ENU}$ as defined by Eq. (6). The final subtraction in Eq. (6) shifts the position in the topocentric frame to the Earth's surface. By this description, the slant range vector $\mathbf{X}_{ENU}$ is described in a topocentric rotating frame in which the effect of the Earth's oblateness is also included. The components of the slant range vector can be written as:

$$x_{ENU} = (R_E + h)[c(\theta)c(\Omega - \lambda) + s(\theta)s(\Omega - \lambda)c(i)] \tag{16a}$$

$$y_{ENU} = (R_E + h)[-(c(\theta)c(\Omega - \lambda) - s(\theta)s(\Omega - \lambda)c(i))s(\phi) + s(\theta)s(i)c(\phi)] \tag{16b}$$

$$z_{ENU} = (R_E + h)[(c(\theta)c(\Omega - \lambda) - s(\theta)s(\Omega - \lambda)c(i))c(\phi) + s(\theta)s(i)s(\phi)] - R_E \tag{16c}$$

where s and c are the sine and cosine functions, and λ and ϕ are the longitude and the latitude of the solar power farm, respectively. Due to the Earth's rotation, λ is equal to:

$$\lambda = \lambda_o + \omega_E t \tag{17}$$

with λ_o the initial position of the solar power farm in the ECI frame, and ω_E is the Earth's rotation rate, as noted earlier. The magnitude of the slant range can be calculated as $d = || \mathbf{X}_{ENU} || = \sqrt{x_{ENU}^2 + y_{ENU}^2 + z_{ENU}^2}$, such that:

$$d = \sqrt{(R_E + h)^2 - 2R_E(R_E + h)[c(\theta)c(\Omega - \lambda)c(\phi) - s(\theta)s(\Omega - \lambda)c(i)c(\phi) + s(\theta)s(i)s(\phi)] + R_E^2} \tag{18}$$

For a polar orbit and non-rotating Earth ($\omega_E = 0$) and an equatorial solar power farm at $\phi = 0$ deg at $\lambda_o = 90$ deg, the above expression would take the following form:

$$d = \sqrt{(R_E + h)^2 + R_E^2 - 2R_E(R_E + h)\cos(\theta)} \tag{19}$$

which is the same as the scalar formulation of the slant range in Çelik and McInnes (2022), where the cosine rule is used to derive the slant range.

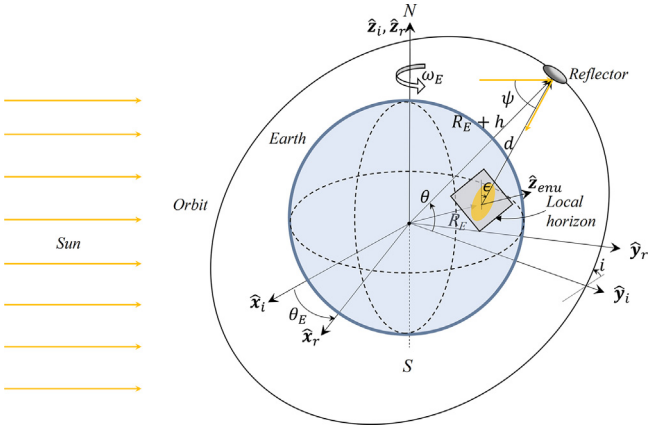

Fig. 2. Geometry during an orbital pass. Image not to scale.

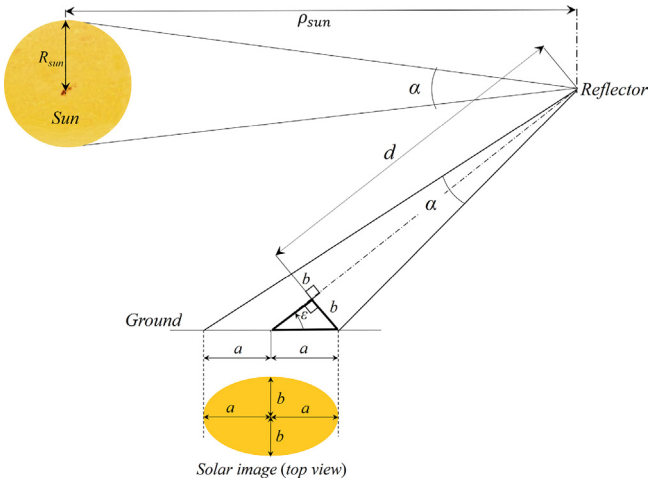

Fig. 3. Geometry of the reflected image from a side view (adapted from Çelik and McInnes (2022)). The reflector is assumed point-like in this paper. Image not to scale.

The analytical slant range expression defined by Eq. (18) can now be tested against a numerical simulation. Because the J_2 effect is included in the description, a circular Sun-synchronous orbit (SSO) at 1000 km altitude is going to be considered. The orbit inclination can be found from Eq. (11) by setting $\dot{\Omega}$ the Earth's orbit rate around the Sun (i.e., $\omega_{\odot} = 1.992 \times 10^{-7}$ rad s^{-1}) and is found to be $i = 99.48$deg. The initial right ascension of the ascending node is selected as $\Omega_0 = 90$deg. The solar power farm is equatorial ($\phi = 0$) and is initially on the terminator line at $\lambda_o = 90$deg. The selection of orbit and solar power farm parameters means that the reflector is at the zenith point and the slant range is equal to its orbit altitude h. The analytical slant range values are generated for a 24 hour time period with 1-s time intervals. These values are compared against the slant range computed from a numerically simulated orbit with the same orbit and solar power farm parameters. The results are presented in Fig. 4 below.

Fig. 4 demonstrates the general agreement between the analytical description and the numerical simulations. The minimum possible slant range is 1000 km for this orbit and it occurs at the beginning of the simulation as described earlier. The slant range then follows a sinusoidal-type structure with varying amplitudes due to the Earth's rotation, with values between approximately 1000 km and slightly less than 14000 km. If the Earth was non-rotating, the slant range value would be varied between the minimum possible value (1000 km) and the maximum possible value (twice the orbit radius) as the reflector orbits around the Earth.

The error between the analytical and numerical values is within 0.3% and mostly less than 0.1%, as shown in the right panel of Fig. 4. As discussed earlier, the J_2 effect on the other orbital parameters is generally negligible but may still introduce errors. For example, the orbit radius varies by approximately 15 to 20 km as a result of the Earth's oblateness, even though the net change over one orbit period is zero. This variation within an orbit corresponds to 0.27%. The second zonal harmonic description of the Earth's oblateness also introduces errors in the slant range as compared to fully numerical simulations. However, approximately a minimum of 99.7% agreement is deemed acceptable for the current model.

The slant range expression in Eq. (18) can now be used in combination with its z component to find the elevation, ϵ, which can be expressed as:

$$\epsilon(t) = \arcsin \frac{z_{ENU}(t)}{d(t)} \tag{20}$$

In addition to the image size, this elevation expression will also be useful in finding the start and end points of a pass, as $\epsilon = 0$ deg and $\epsilon = 180$ deg mark those points respectively. This will be demonstrated in the following subsections.

Finally, the angle subtended by the Sun, α, can be calculated as a function of the distance between the Earth and the Sun, and the radius of the Sun according to Fig. 3, expressed as follows:

$$\alpha = 2 \arctan \frac{R_{sun}}{\rho_{sun}} \tag{21}$$

where R_{sun} denotes the radius of the Sun, i.e., 696500 km (Giorgini, 2015), and ρ_{sun} denotes the distance from the Sun, as shown in Fig. 3. Substituting R_{sun} and the mean Earth–Sun distance 1 Astronomical Unit (AU) would result in α as 0.0093rad. With all the necessary parameters described, one can now express the area of the elliptical solar image in Fig. 3 as (Çelik and McInnes, 2022):

$$A_{im}(t) = \pi a(t) b(t) = \pi \frac{[d(t) \tan(\alpha/2)]^2}{\sin \epsilon(t)} \tag{22}$$

After substituting for the elevation expression from Eq. (20) in Eq. (22), this becomes:

$$A_{im}(t) = \frac{\pi d(t)^3 \tan(\alpha/2)^2}{z_{ENU}(t)} \tag{23}$$

Note that Eqs. (21)–(23) assume a point-like reflector, as also shown in Fig. 3. The effect of the finite size of the reflector is negligible when the reflector size is small compared to the orbit altitude. Çelik and McInnes (2022) estimated that for a 1 km diameter reflector at 1000 km altitude, the contribution of the finite reflector size is approximately 0.5% to the total solar image area (Çelik and McInnes, 2022). Therefore it is neglected in this paper, but it should be taken into account when the reflectors are much larger and/or the altitude is low. The calculation of the area of the solar image is an important part of the energy delivery process which will be discussed next.

4. A model for reflected solar energy delivery from space

The energy collected by an orbiting solar reflector with area A_{ref} is delivered across an image area $A_{im}(t)$ during

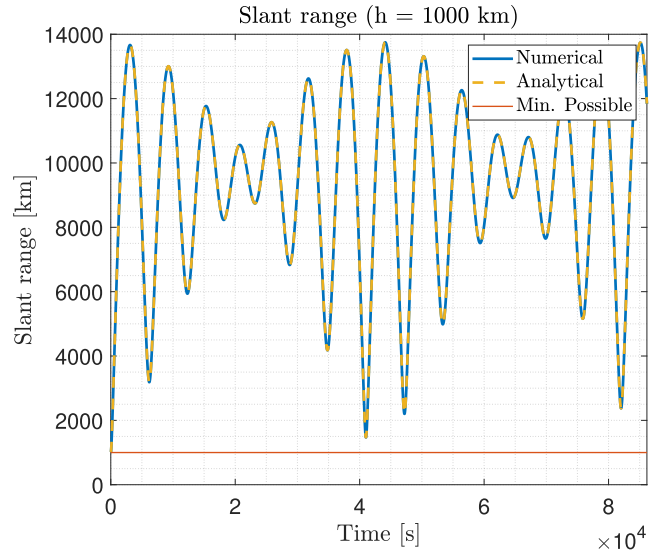

(a) Slant range

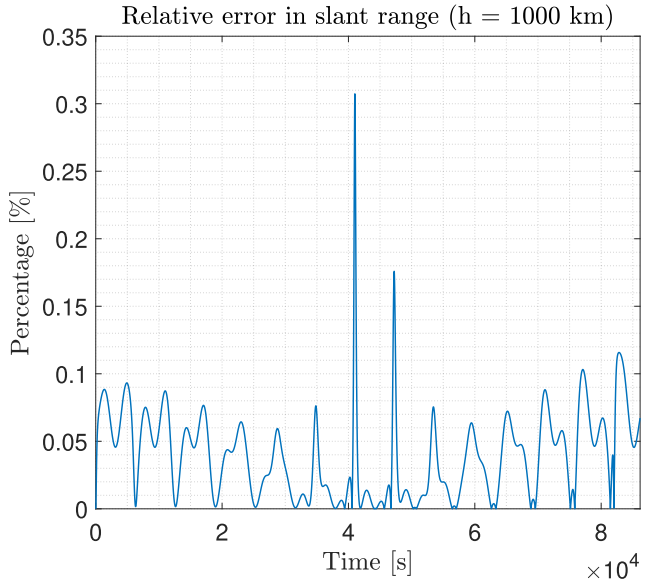

(b) Relative error

Fig. 4. The semi-analytically generated slant range compared against a numerically simulated orbit.

an orbital pass. The power density, σ on the ground can be expressed by the following relationship (Çelik and McInnes, 2022):

$$\sigma = \tau(t) I_o \frac{A_{ref}}{A_{im}(t)} \cos\frac{\psi(t)}{2} \tag{24}$$

where I_o is the solar constant that is assumed to follow an inverse-square law with distance from the Sun and is equal to 1370 W m^{-2} at 1 AU. $\psi(t)$ is the angle between the incoming and the reflected sunlight, i.e. the angle of incidence, as shown in Fig. 2. $\tau(t)$ is an atmospheric loss function. Multiplying Eq. (24) by the effective area of the solar power that utilises the illumination results in the received solar power on the ground as:

$$P = \sigma A_{eff}(t) = \tau(t) I_o \frac{A_{ref} A_{eff}(t)}{A_{im}(t)} \cos\frac{\psi(t)}{2} \tag{25}$$

where $A_{eff}(t)$ is the effective solar power farm area, which will be shown to be time-dependent for finite-sized solar power farms as the solar image varies with elevation. Equation (25) expresses the concept of orbiting solar reflectors in mathematical terms, in which an orbiting solar reflector with area A_{ref} intercepts incoming sunlight and reflects it onto an area on the ground, $A_{im}(t)$ by an angle of incidence $\psi(t)$. The projected sunlight is then captured on the ground by an area $A_{eff}(t)$ to be utilised. The intensity of the sunlight is reduced as it transmits through the atmosphere by a function τ. One can then determine the total energy delivered by integrating Eq. (25) over the duration of the orbital pass such that:

$$\begin{aligned} E = \int_0^{T_{pass}} P \mathrm{d}t &= I_o A_{ref} \int_o^{T_{pass}} \tau(t) \frac{A_{eff}(t)}{A_{im}(t)} \cos\frac{\psi(t)}{2} \mathrm{d}t \\ &= \frac{I_o A_{ref}}{\pi \tan(\alpha/2)^2} \int_0^{T_{pass}} \tau(t) \frac{A_{eff}(t) z_{ENU}(t)}{d(t)^3} \cos\frac{\psi(t)}{2} \mathrm{d}t \end{aligned} \tag{26}$$

where T_{pass} denotes the orbital pass duration. Even though all terms can be expressed analytically, the only analytical solution to the integral in Eq. (26) is in the form of elliptical integrals and available when τ, A_{eff} and ψ are all constants (Çelik and McInnes, 2022). Such a solution may be useful for non-terrestrial applications (such as for the Moon), but the modelling for terrestrial applications will require a numerical solution. Even before obtaining a solution, one may deduce insights into the energy delivery process. At the beginning and end of the pass, A_{im} will be infinite hence the power delivered will start from zero, gradually increasing until A_{im} becomes its smallest value where the solar power density is the highest, and decreasing again as A_{im} grows to infinity. However, while such a qualitative description is rather straightforward, the modelling of solar energy delivery for a generic orbit when the Earth's rotation and orbit around the Sun are both included will pose a non-trivial modelling problem. One of those is the calculation of the orbital pass duration, which will be discussed next.

4.1. Detection of pass duration

The inclusion of the Earth's rotation and generic orbit properties means that the pass duration is a function of the position of the solar power farm. The pass duration may then be sought by using the analytical slant rage expression, particularly its z-component or the reflector height from the local horizon plane.

Two different approaches are considered in this paper to find the pass duration. The first one is to use one of the properties of z_{ENU}, i.e., z_{ENU} can only be positive when the reflector is above the local horizon or in view by the solar

power farm. A z_{ENU} profile can then be generated similar to the slant range profile in Fig. 4 and the time points at which z_{ENU} is positive can be identified. To do the latter, a detection algorithm is developed, in which the switch from negative to positive values (or vice versa) of z_{ENU} is detected and the zero crossing is identified by interpolating between the two positive and negative values. The difference between the time points of zero crossings will then be the pass duration. A particular advantage of this approach is the ability to detect daily passes over a given solar power farm and their pass duration. This may be useful, for example, for the scheduling of solar power farms to be serviced by the reflectors during the day. Fig. 5 depicts an example of this for the orbit considered in the previous section.

Fig. 5 shows all the detected passes regardless of their elevation. The maximum possible z_{ENU} is 1000 km and corresponds to the minimum slant range. The other passes have lower z_{ENU} values and are therefore not overhead. The first detection, which corresponds to a half pass, occurs at 0.145 h, meaning that the full pass would last 0.29 h or 17.4 min. In the spherical and non-rotating Earth model, the pass duration will be 17.62 min. The subsequent passes last for a shorter duration, 9.62 min, 16.66 min, 14.65 and 14.08 min, respectively. Shorter duration passes are expected in the subsequent passes as they occur at lower elevations (due to lower z_{ENU}).

Alternatively, pass duration may be found by using the elevation expression. ϵ needs to be 0 deg and 180 deg when the reflector rises and sets, respectively. This would also be the point where z_{ENU} is equal to zero from Eq. (20) such that:

$$\epsilon = \arcsin\frac{z_{ENU}}{d} = 0 \Rightarrow \frac{z_{ENU}}{d} = 0 \Rightarrow z_{ENU} = 0.$$

As the pass begins at this point, it can be assumed for convenience that $t = 0$, such that

$$z_{ENU}(0) = 0 \tag{27}$$

This nonlinear equation can be solved to find the initial argument of latitude, θ_o for a given initial position of the solar power farm, λ_o. Once θ_o is found, it can be input again into the same z_{ENU} equation, but this time evaluated at some $t = T_{pass}$, such that:

$$z_{ENU}(T_{pass}) = 0 \tag{28}$$

This second nonlinear equation can be solved to find T_{pass}. Note that despite the equations being the same, the first one is solved for the initial orbital position, whereas the second is solved to find the pass duration. As a demonstration of a simplified case, one may consider a circular polar orbit ($i = 90$deg) and an equatorial solar power farm at (i.e., $\phi = 0$). At $t = 0$, z_{ENU} in Eq. 16 would become as follows:

$$z_{ENU}(0) = (R_E + h)[c(\theta_o)c(\Omega - \lambda_o)] - R_E = 0 \tag{29}$$

then θ_o can be found as

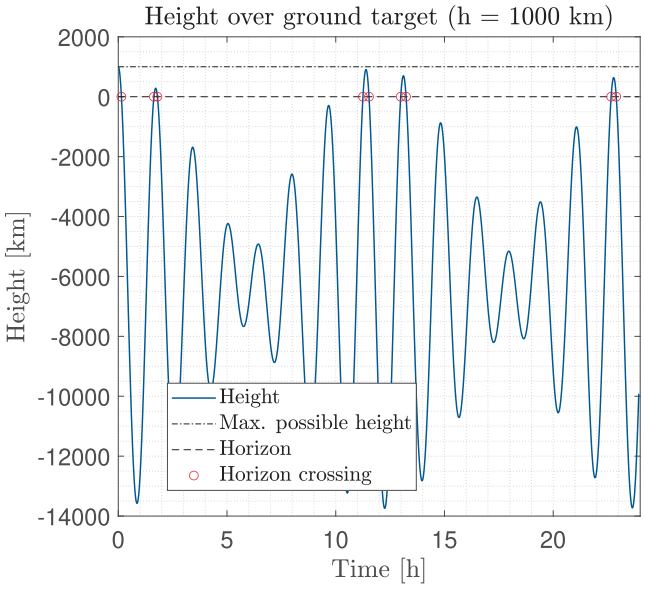

Fig. 5. Estimating pass duration by detecting horizon crossing.

$$\theta_o = \arccos\left(\frac{R_E}{\cos(\Omega - \lambda_o)(R_E + h)}\right) \tag{30}$$

Then, substituting θ_o in z_{ENU} in Eq. 16 again at some $t = T_{pass}$ and rearranging would yield

$$\begin{aligned} &\cos(\theta_o + \omega_o T_{pass})\cos(\Omega - (\lambda_o + \omega_E T_{pass})) = \tfrac{R_E}{(R_E+h)} \\ &\quad\Rightarrow \cos(\theta_o - \Omega + \lambda_o + (\omega_o - \omega_E)T_{pass}) \\ &+\cos(\theta_o + \Omega - \lambda_o + (\omega_o + \omega_E)T_{pass}) = \tfrac{2R_E}{(R_E+h)} \end{aligned} \tag{31}$$

which can be solved to find T_{pass}. Further simplifications can be made if the orbit is a repeating ground track (RGT), where $\omega_E = \eta\omega_o$ (η is an integer). However, despite the analytical description, an exact T_{pass} will likely be found numerically, even for a simple case such as this. The solutions are obtained through MATLAB's `fzero` function in this paper, which finds the root of a nonlinear function (Forsythe et al., 1977). The initial conditions required by the function may be obtained through the non-rotating Earth assumption with an overhead pass (Çelik and McInnes, 2022). In that case, the half angle determines the point where the reflector rises above the local horizon, which can be used to find θ_o. It is expressed as:

$$\beta = \arccos\frac{R_E}{R_E + h} \tag{32}$$

where β denotes the half angle. Note the similarity between Eq. (32) and Eq. (30). The initial condition for the second equation would be the pass duration in the same non-rotating Earth case with an overhead pass, such that:

$$T_{pass,sta} = \frac{2\beta T}{2\pi} = \frac{T}{\pi}\beta \tag{33}$$

where T is the orbit period.

The detection of the pass duration by this approach may be more suitable for individual solar power farm passes. To

that end, the orbit considered in the previous section is again used to demonstrate this approach with several different initial solar power farm positions. The results are tabulated in Table 1.

Recall that at this altitude, the pass duration is calculated as 1057.4 s or 17.62 min for non-rotating solar power farms. The maximum pass duration is found at $\lambda_o = 88$ deg with 1041.76 s, which is approximately 15 s less than the idealised case, meaning a near-overhead pass. It may be noticeable from Table 1 that for the day-side λ_o (i.e., $\lambda_o < 90$ deg), T_{pass} is generally higher than for the night-side λ_o. This is because the eastward rotation of the Earth means that the reflector and the solar power farm are approaching each other in the former case in the retrograde orbital motion, whereas in the latter the solar power farm moves away from the reflector. This can be better observed from the elevation profiles of these passes as provided in Fig. 6.

The differences in the pass duration can be observed from the end points of time in the x-axis Fig. 6. As expected, the higher the elevation is, the closer the pass duration is to a non-rotating Earth case. The elevation reaches almost 90 deg for $\lambda_o = 88$ deg. There are also two pairs of cases where the maximum elevation is similar. These are 84–92 deg and 80–96 deg cases with values on each side of the terminator line which yield elevation values of approximately 60 deg and 40 deg at the maximum, respectively. The smallest values in the pairs are farther away from the terminator line than the largest values. The farthest case, $\lambda_o = 100$ deg, yields the lowest elevation as expected. As for the slant ranges shown in the right panel, the near-overhead pass means that the slant range is approximately equal to the orbit altitude at the zenith point. The slant range for $\lambda_o = 88$ deg case is 1000.2 km, only approximately 200 m higher than the orbit altitude. The minimum slant range is higher for other λ_o values, as expected in offset passes.

The method in this paper is developed to avoid any additional numerical orbit propagation to detect the variable pass duration. It also provides insights into the variation of the pass duration as a function of the initial reflector and solar power farm positions, even though the final equation to be solved is nonlinear. However, it is also of interest how this methodology compares against numerical simulations. To that end, the results of this paper will be compared against two numerical tools, a J_2-enhanced two-body orbit propagator, customised to calculate the quantity of energy delivered (Viale et al., 2022) and the contact locator functionality of General Mission Analysis Tool (GMAT), developed by NASA and their collaborators.[1] Again, a 1000 km altitude circular SSO, placed at the terminator line is considered. In addition to the inclination for this altitude ($i = 99.5$deg), 0, 45, 90, 135, 180 deg

[1] Available at https://sourceforge.net/projects/gmat/ (Accessed March 7, 2023).

Table 1
Pass duration for equatorial solar power farms at different initial points measured from the inertial frame at 1000 km altitude Sun-synchronous orbits placed on the terminator line

λ_o [^{o}]	T_{pass} [s]
80	1009.19
84	1034.17
88	1041.76
92	1032.91
96	1007.47
100	964.17

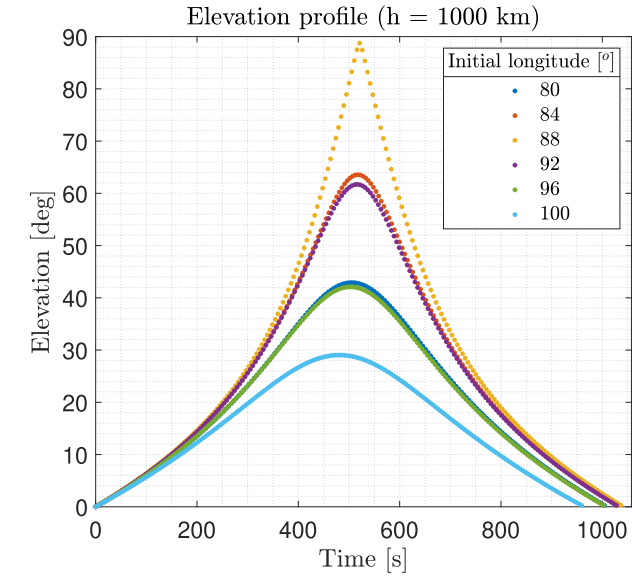

(a) Elevation

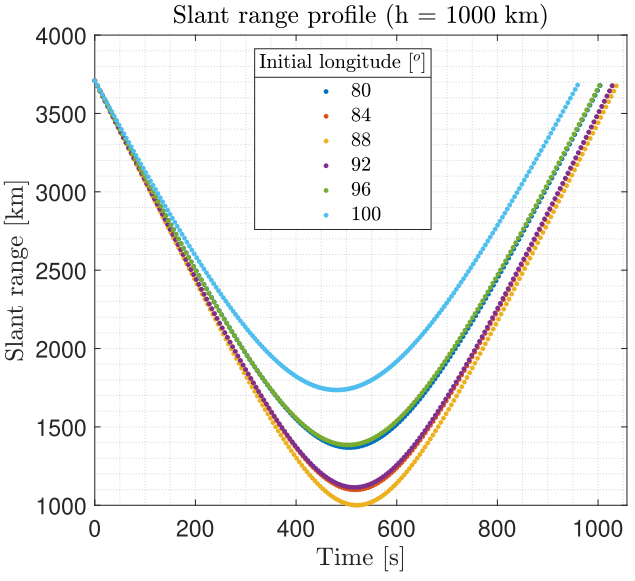

(b) Slant range

Fig. 6. The elevation and the slant range profiles in the 1000 km SSO case for different initial solar power farm positions.

inclinations are also considered to compare against a wide variety of orbits that are both prograde and retrograde. The equatorial solar power farm is given an initial longitude of $\lambda_o = 90$ deg. The corresponding θ_o is calculated by the steps outlined earlier in this subsection and inputted to GMAT as the initial condition to make the calculations as close as possible to this study. Similarly, the Earth's radius, gravitational parameter (μ) and the J_2 constants are also taken to be the same as GMAT and inputted to semi-analytical and numerical simulations. The results are presented in Table 2.

There is generally a good agreement between all techniques, albeit differences at different inclinations. The strategy presented in this paper and the two-body orbit propagation display an agreement within 3 s. The difference with GMAT is higher but generally within 30 s for all cases. The difference decreases to within 15 s for equatorial orbits. The exact reason for the discrepancy between the semi-analytical technique in this paper and GMAT is not clear, especially given that the same constants are used for the parameters such as J_2. However, it is found that the GMAT results are sensitive to the initial epoch of the simulation, which may be a reason to explain the discrepancy. It is important to note that this discrepancy may not be detrimental as such, as the quantity of energy delivered at the beginning or the end of a pass constitutes only a small fraction of the total quantity, as shown in Çelik and McInnes (2022), and will also be shown later in this paper. The conditions such as eclipses may have a greater impact on the effective pass duration, which will be investigated in the next subsection.

Table 2
The results of pass duration (T_{pass}) at 1000 km altitude circular orbit at different inclinations in this paper, compared against J_2-enhanced two-body orbit propagation and NASA's GMAT.

i [deg]	This paper	Numerical	GMAT
0	1139.46	1137.48	1123.76
45	1111.79	1008.22	1038.78
90	1052.95	1051.31	1025.12
99.5 (SSO)	1040.57	1042.69	1014.61
135	1002.92	999.60	987.78
180	984.20	982.37	982.26

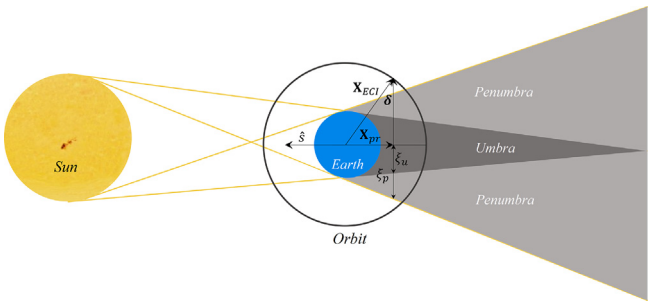

Fig. 7. Generic eclipse geometry (Adapted from (Longo and Rickman, 1995)). The details of the calculation of ξ_p and ξ_u can be found in Appendix B. Image not to scale.

4.2. Eclipses

Eclipses may need to be considered if there is a significant deviation from near-polar orbit inclinations, when the right ascension of the ascending node or initial solar power farm longitudes are further into the night side or when all these occur. The existence of eclipses shortens the duration of the orbital pass where solar energy can be delivered, as the incoming sunlight to the reflector is blocked by the Earth's shadow cone, as shown in Fig. 7.

Whether there is any eclipse in an orbit can be calculated by projecting the current reflector position in orbit $\mathbf{X}_{ECI}$ onto the unit Sun vector, such that (Longo and Rickman, 1995):

$$\mathbf{X}_{pr} = (\mathbf{X}_{ECI} \cdot \hat{s})\hat{\mathbf{s}} \tag{34}$$

where $\mathbf{X}_{pr}$ is the projected reflector position and $\hat{s}$ is the unit Sun vector, such that $\hat{s} = \frac{\mathbf{X}_{sun}}{||\mathbf{X}_{sun}||}$. If $(\mathbf{X}_{ECI} \cdot \hat{s}) < 0$, the point of the shadow cone entry (both for penumbra (partial eclipse) and umbra (total eclipse)) may be found (Longo and Rickman, 1995). Another vector can be defined to find this point as:

$$\delta = \mathbf{X}_{ECI} - \mathbf{X}_{pr} \tag{35}$$

If $||\ \delta\ ||$ is smaller than ξ_p or ξ_u in Fig. 7, the reflector will be in penumbra or umbra, respectively (Longo and Rickman, 1995). Only umbra cases are considered in this paper, therefore ξ_u is found as follows (Longo and Rickman, 1995):

$$\xi_u = (\rho_u - ||\ \mathbf{X}_{pr}\ ||) \tan \alpha_u \tag{36}$$

where ρ_u denotes the height and α_u is the apex angle of the umbra cone. The details of the calculation are given in Appendix B.

For the problem at hand, the time at which the reflector is in eclipse can be calculated, after the pass duration is found. There are three different eclipse cases that may occur (other than no eclipse), which are eclipse at the beginning of the pass, towards the end of the pass, and in the middle of the pass, as shown in Fig. 8. Depending on retrograde or prograde motion, the first two cases would occur at dawn or dusk passes, whereas the third case may occur if the pass duration is very long, particularly later at night time for higher altitude orbits.

Incorporating eclipses into the problem will further divide the piecewise integration which will be discussed later, depending on which case of geometric loss where the eclipse occurs, and when the eclipse occurs (i.e., beginning, end or middle of the pass). Such an approach may be cumbersome in implementation. In this paper, this was avoided by integrating Eq. (26) first for the full duration of the pass $[0, T_{pass}]$. Then, the same integration is performed for the eclipsed part of the pass between some ini-

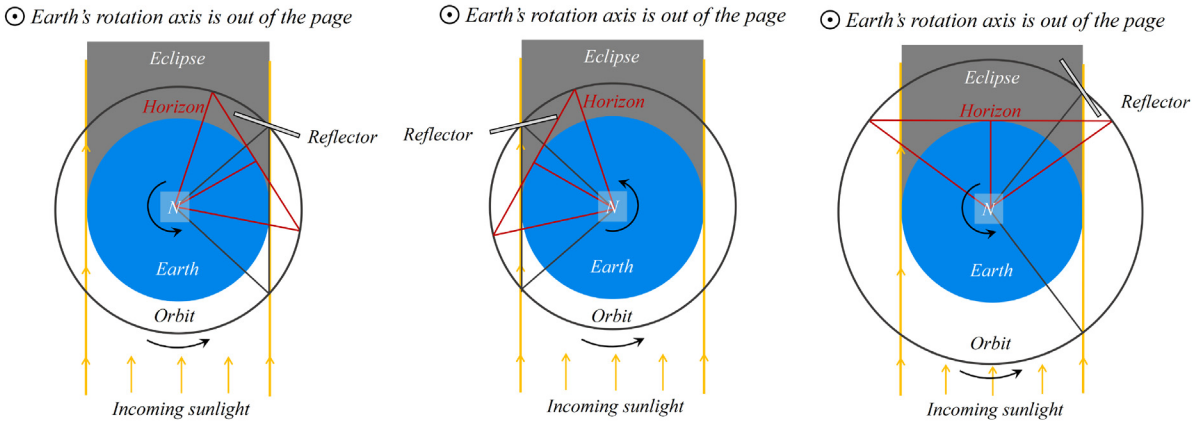

(a) End of pass (b) Beginning of pass (c) Middle of pass

Fig. 8. Eclipse cases that may occur during a pass. The red triangle shows a projection of the cone extending from the centre of the Earth and defines the local horizontal plane of a solar power farm. Depending on the initial position of the solar power farm at the beginning of a pass and orbit altitude, the reflector may be in the Earth's shadow (a) towards the end, (b) at the beginning and (c) in the middle of the pass. Cases (a) and (b) are more likely to occur for lower altitude orbits whereas case (c) would likely occur for much higher altitude orbits. Image not to scale.

tial time $T_{ecl,0}$ and the final time $T_{ecl,f}$. Finally, the quantity of energy "delivered" in the eclipsed part is subtracted from the quantity of energy delivered in the no-eclipse case to calculate the net energy delivery in the pass.

As the calculation of the eclipse entry and exit points is algebraic, the eclipse evaluation can be done offline, i.e., before the integration. The eclipse time points can be calculated and assessed when in the pass the eclipses occur (i.e, towards the beginning, end or middle of the pass). After the no-eclipse integration, all the necessary information for the eclipse part, such as geometric losses to be considered (which will be explained in more detail in the next section), will already have been calculated. This information can be used to assess which piecewise integrals need to be solved for the eclipse part. Fig. 9 demonstrates how the eclipse-free part of the total pass duration is altered for a Sun-synchronous orbit at 1000 km altitude, for a range of orbit inclinations and initial solar power farm longitudes for an equatorial farm.

The left panel in Fig. 9 shows pass duration when eclipses are omitted. It shows an approximately symmetric profile around 88deg where lower inclination orbits result in longer pass duration as their motion is prograde. As the inclination increases and the motion becomes retrograde (i.e., i >90deg), the pass duration decreases. The results presented in the previous section can also be identified in the left panel, where for a 1000 km SSO at $i = 99.5$ deg Ω=90 deg, the pass duration is higher for λ_o at approximately 88 deg, and decreases before and after this point. When the eclipse loss is included, its effect is visible when λ_o >90 deg and when the orbit inclination is outside the range of 60 deg $< i <$ 120 deg. When the solar power farm is initially further into the night, near-equatorial orbits lose nearly half of their effective pass duration. This is true for both prograde and retrograde orbits. The results in Fig. 9 do not show any eclipses in the middle of pass, and due to the selected range of λ_o, the prograde orbits experience eclipses towards the end of the pass and the retrograde orbits in the beginning. The losses due to eclipses may have a significant impact on solar energy delivery. However, if the eclipses are short and at the beginning or end of a pass, the quantity of energy lost may be negligible, but the loss may be significant if it is in the middle of a pass, where the quantity of the energy delivered is the highest, or if the eclipse duration is long. This can be assessed in the model with the offline eclipse check. During the solar energy delivery process, further losses will be experienced due to the finite size of the solar power farm, which is discussed in the next subsection.

4.3. Effective solar power farm area

As shown in Section 3, the shape of the solar image is elliptical (with the exception of the zenith point, where it is circular) and its exact shape is dependent on the time-varying slant range and elevation. For a solar power farm, this will mean that only the portion of the farm illuminated can be used for electricity generation. This will be termed as the effective area, or A_{eff}. This will then make the interaction between the areas of the solar power farm and the solar image important to model for the accurate estimation of the solar energy delivered. To that end, the solar power farm is modelled as disks on the ground. While this is evidently not an accurate description of a solar power farm, it will be used as a test case to demonstrate the modelling of A_{im}.

Under the assumption of the solar power farm area as a disk, three distinct geometric cases can be identified, as shown in Fig. 10. These will be explained below:

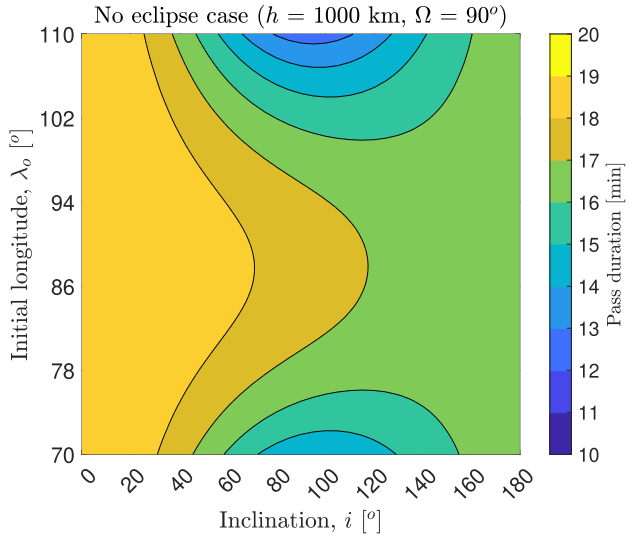

(a) Pass duration without eclipses

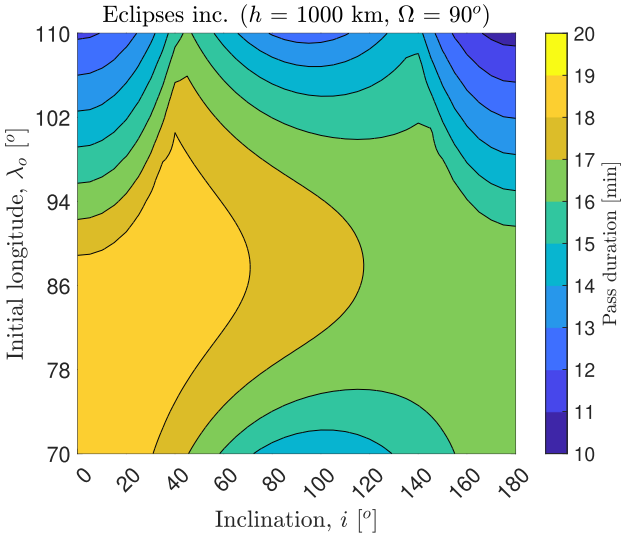

(b) Pass duration with eclipses

Fig. 9. Pass duration with or without eclipses included for 1000 km Sun-synchronous orbit at a range of inclinations and initial equatorial solar power farm longitudes.

1. The semi-minor axis length, b, of the solar image is equal to or greater than the solar power farm radius, R_{gt}, i.e. $b \geqslant R_{gt}$. This means that the solar power farm is fully illuminated by the solar image, $A_{eff} = A_{gt} = \pi R_{gt}^2$.
2. The semi-major axis length, a, of the solar image is equal to or smaller than the solar power farm radius, R_{gt}, i.e. $a \leqslant R_{gt}$. This means that the area of the solar image is equal to the area illuminated, $A_{eff} = A_{im} = \pi a(t) b(t)$.
3. The solar power farm radius, R_{gt}, is greater than b but smaller than a, i.e., $b < R_{gt} < a$. This means that the solar power farm is illuminated only by a portion of the solar image, defined by the area intersecting between the solar power farm disk and the solar image ellipse. This case requires a more detailed geometric analysis, which is provided in Çelik and McInnes (2022). Here, only the expression describing this area will be provided as follows:

$$A_{eff} = 4\left[\frac{\gamma}{2}R_{gt}^2 + \frac{\pi b^2}{4\sin\epsilon} - \frac{b^2}{2\sin\epsilon}\arctan\frac{\tan\gamma}{\sin\epsilon}\right] = 2\gamma R_{gt}^2 + \frac{2b^2}{\sin\epsilon}\left[\frac{\pi}{2} - \arctan\frac{\tan\gamma}{\sin\epsilon}\right] \tag{37}$$

where γ is a polar angle defined at the intersection point of the solar power farm disk and the solar image ellipse, shown in the middle figure in the top row of Fig. 10.

Note that while these are the different cases that may be encountered, not all of them are encountered for each pass. For the non-rotating Earth case tackled in Çelik and McInnes (2022), these cases can be determined based on a limiting altitude, beyond which only Case 1 occurs. However, this is much more complicated in the current model and depends also on the longitudinal separation between the solar power farm and the reflector. Each of the above cases may occur by itself during a pass, or they may occur in pairs or all together.

In the implementation, b and a are generated for discrete time points of the orbital pass and it is checked whether b and a become smaller than R_{gt} at any point during the orbital pass, before investigating individual A_{eff} cases. If b never becomes smaller than R_{gt}, then Case 1 occurs, if both b and a become smaller than R_{gt} at some point in the pass, then all three cases will occur. In order to accurately estimate the times at which the transition occurs from Case 1 to 2 and Case 2 to 3, the root of the following equations are found:

$$\mathrm{f}_b(t) = b(t) - R_{gt} = d(t)\tan(\alpha/2) - R_{gt} \tag{38a}$$

$$\mathrm{f}_a(t) = a(t) - R_{gt} = \frac{b(t)}{\sin\epsilon(t)} - R_{gt} \tag{38b}$$

The times, t_b, t_a at which $\mathrm{f}_b(t_b) = 0, \mathrm{f}_a(t_a) = 0$ mark the transitions. Note that there will be pairs of t_b and t_a. For $t_b, t_{b,0}$ is the first instance where $b = R_{gt}$ after the reflector rises above the horizon, whereas $t_{b,f}$ is the second instance where the same identity occurs, shortly before the pass ends. The same is more straightforward for t_a where $t_{a,0}$ and $t_{a,f}$ mark the first and the last time points, respectively, where $a = R_{gt}$. In the implementation, the solutions are again obtained by `MATLAB`'s `fzero` function (Forsythe et al., 1977). It was observed that solving these equations may present challenges if the time points are very close to each other, albeit rare for practical cases. The initial condition then needs to be carefully selected. The generated b and a values as described above are used to select initial conditions. Again, the discrete time point when b or a is smaller than R_{gt} can be selected and inputted to the `fzero` function as an initial condition. Then, the exact time point (within the numerical tolerance) will be the solution for t_b or t_a. This approach is found to ensure numerical stability.

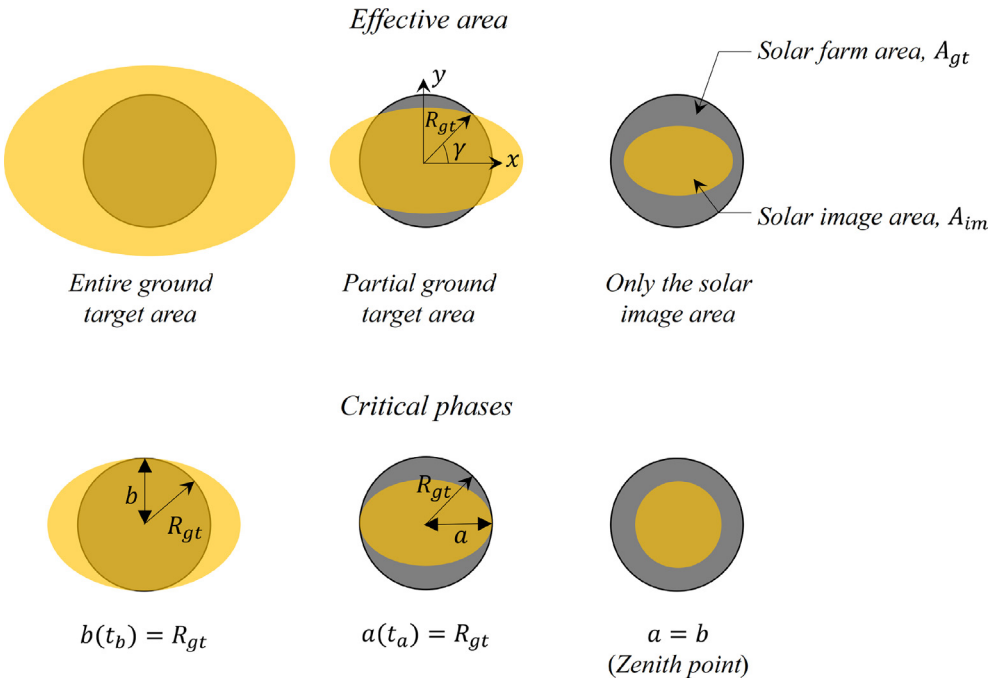

Fig. 10. Three distinct cases of the solar image area in relation to the solar power farm area. Top figure shows effective usable area of the solar power farm in each case considered. Lower figure shows the critical phases of a pass that is used to separate energy integration. At time t_b and t_a, the semi-minor (b) and semi-major (a) axes dimensions of the solar image become equal to the solar power farm radius, respectively. At the zenith point (if it occurs), a and b are equal to each other, i.e., the solar image is circular.

It is also worth noting that the times between $t_{b,0}$ and $t_{a,0}$, and $t_{a,f}$ and $t_{b,f}$ are when Case 3 occurs, which can be found by finding t_b and t_a when both cases occur or t_b or t_a if only one of them occurs. If neither t_b nor t_a is available, then the entire pass is characterised by Case 3.

After the effective solar power farm area and time expressions for each phase are presented, the following conditions can be defined for a pass where all cases occur:

$$A_{eff} = \begin{cases} \pi R_{sf}^2, & t \in [0, t_{b,0}]; t \in [t_{b,f}, T_{pass}] \\ \pi a(t) b(t), & t \in [t_{a,0}, t_{a,f}] \\ \text{Eq. 37}, & t \in (t_{b,0}, t_{a,0}); t \in (t_{a,f}, t_{b,f}) \end{cases} \tag{39}$$

Eq. (39) means that the energy integral in Eq. (26) would need to be solved piecewise between the identified time points and modified accordingly. A detailed discussion on this issue is provided in Çelik and McInnes (2022). It is also worth noting that the solar panel orientation would further divide the energy integral. This case would be most relevant to the tilted photovoltaic panels of a solar power farm. Any non-zero panel tilt would shorten the pass duration and the reflector would illuminate the "backside" of the panels beyond the equivalent elevation angle. Depending on which case this occurs the piecewise integration can be divided further, yielding nine different integrals (Çelik and McInnes, 2022). In the current model, the panel tilt is not implemented to avoid a complexity that adds little value, and the solar panels are assumed parallel to the local horizontal. Instead, one may calculate the effective pass duration (shortened T_{pass} due to the panel tilt) separately and calculate the energy delivered.

4.4. The angle of incidence

The angle of incidence, ψ, is the angle between incoming and outgoing light rays to and from the reflector. The incoming vector is dependent on the position of the Sun and the outgoing vector is dependent on the reflector position with respect to the solar power farm. Both of these vectors are in principle time-varying, although the variation of the position of the Sun may be negligible for short duration passes. Therefore, ψ is a time-varying function and can be expressed as follows:

$$\psi(t) = \arccos\left(\frac{\mathbf{X}_{ref} \cdot \hat{s}}{||\,\mathbf{X}_{ref}\,|| \cdot ||\,\hat{s}\,||}\right) \tag{40}$$

where $\mathbf{X}_{gt}$ and $\hat{s}$ are the position of the reflector with respect to the solar power farm and the unit vector of the Sun, both of which are in the ECI frame. Moreover, $\mathbf{X}_{ref}$ can be expressed as:

$$\mathbf{X}_{ref} = \mathbf{X}_{gt} - \mathbf{X}_{ECI} \tag{41}$$

where $\mathbf{X}_{gt}$ is the instantaneous solar power farm position in the ECI frame such that:

$$\mathbf{X}_{gt} = R_E \begin{bmatrix} \cos\phi \cos\lambda(t) \\ \cos\phi \sin\lambda(t) \\ \sin\phi \end{bmatrix} \tag{42}$$

and $\mathbf{X}_{ECI}$ is the orbital position of the reflector.

The unit Sun vector $\hat{s}$ in equatorial coordinates can be expressed as:

$$\hat{s} = \begin{bmatrix} \cos\theta_{\odot}(t) \\ \cos\xi \ \sin\theta_{\odot}(t) \\ \sin\xi \sin\theta_{\odot}(t) \end{bmatrix} \tag{43}$$

where ξ is the Earth's axial tilt and equal to 23.44 deg. Moreover, $\theta_{\odot}$ is the argument of latitude of the assumed circular orbit of the Earth around the Sun (though for convenience it is assumed the Sun moving around the Earth) and expressed as:

$$\theta_{\odot} = \theta_{\odot,0} + \omega_{\odot} t \tag{44}$$

where $\theta_{\odot,0}$ is the initial position of the Earth, and $\omega_{\odot}$ is the Earth's orbit rate around the Sun, i.e. $\omega_{\odot} = 1.992 \times 10^{-7}$ rads^{-1}. In addition, $\theta_{\odot,0}$ can be found by assuming the vernal equinox as $\theta_{\odot,0} = 0$, where $\hat{s} = [1, 0, 0]^T$. As the Sun vector points to the direction of 12 o'clock noon, the time in the Greenwich meridian (expressed as an angle) can also be found by using the Sun vector. This may be useful to express the initial position of a solar power farm as the time of the day.

It is worth noting that a trigonometric manipulation may be made to simplify the angle of incidence term in Eq. (26). First, let us consider the following trigonometric identity for some variable v:

$$\cos\frac{v}{2} = \text{sign}\left(\cos\frac{v}{2}\right)\sqrt{\frac{1+\cos v}{2}} \tag{45}$$

Substituting ψ in Eq. (40) into Eq. (45) would yield:

$$\begin{aligned} \cos\frac{\psi}{2} &= \text{sign}\left(\cos\frac{\psi}{2}\right)\sqrt{\frac{1}{2}\left(1+\left(\frac{\mathbf{X}_{ref}\cdot\hat{s}}{||\,\mathbf{X}_{ref}\,||\cdot||\,\hat{s}\,||}\right)\right)} \\ &= \sqrt{\frac{1}{2}\left(1+\left(\frac{\mathbf{X}_{ref}\cdot\hat{s}}{||\,\mathbf{X}_{ref}\,||\cdot||\,\hat{s}\,||}\right)\right)} \end{aligned} \tag{46}$$

as $\psi \in [0, 180]$ deg, hence $\cos\frac{\psi}{2} \in [0, 1]$. Albeit small in individual cases, implementing a trigonometric function in this form could save computational time in large scale optimisation problems.

4.5. Atmospheric losses

Atmospheric losses in this problem include both transmission efficiency through the clear sky and cloudiness. For the former, Hottel (1976) provides an empirical model for atmospheric transmission efficiency that is dependent on the elevation angle (hence time-dependent) from the local horizon (Hottel, 1976):

$$\tau(t) = c_0 + c_1 e^{-k\sec(\pi/2-\epsilon(t))} \tag{47}$$

where c_0, c_1 and k are empirical coefficients. In their work, Hottel (1976) also provides a table of correction coefficients for the sea-level elevation of the solar power farm (up to 2.5 km) and climatic variations, including tropic and arctic weather (Hottel, 1976). This model is discussed in more detail in both Hottel (1976) and Çelik and McInnes (2022). In this paper, the coefficients are selected for a sea-level solar power farm without a climate correction. Eq. (47) then takes the following form (Hottel, 1976; Çelik and McInnes, 2022):

$$\tau(t) = 0.1283 + 0.7559e^{-0.3878\sec(\pi/2-\epsilon(t))} \tag{48}$$

According to Eq. (48), the atmospheric transmission efficiency is equal to 0.641 at the zenith point ($\epsilon = 90$ deg), i.e. approximately 36% of the solar energy is lost to the atmosphere. With the correction coefficients for higher altitudes and possible re-reflection, the efficiency increases to a maximum of 70% according to this model (Hottel, 1976). The efficiency is more than 0.5 for $38\,\text{deg} \leqslant \epsilon \leqslant 142\,\text{deg}$. However, the transmission efficiency decreases further down to approximately 0.13 at the beginning and the end of an orbital pass.

As for cloud cover, there is no available model to incorporate in Eq. (26) to the knowledge of the authors. Therefore, a cloudless sky will be assumed. However, according to different studies, total cloudiness can decrease solar illumination down to a quarter of a clear day and partial cloudiness down to a third of a clear day (Canady and Allen, 1982; Ehricke, 1979; Ehnberg and Bollen, 2005).

4.6. Discussion

In this section, the implementation of the model and its applicability to elliptical orbits will be discussed.

4.6.1. Implementation

The model is implemented in the `MATLAB` environment, but only a few built-in functions are used. The procedure begins with user-input initial conditions such as orbital elements, initial solar power farm position and the Earth's position around the Sun (i.e., the season). Based on this information, the cartesian orbital position of the reflector and slant range from the solar power farm is generated (Section 2 and 3). Next, pass duration (provided that the solar power farm is visible) (Section 4.1), and eclipses (Section 4.2) are calculated offline, i.e. before the energy integration begins. Eclipse cases are given distinct case numbers to identify which type of eclipse occurs (Fig. 8). Given the discrete time points in a pass, transition time points between different geometric relationships between the solar power farm and the solar image (Fig. 10) can also be generated offline, which can be refined by solving nonlinear equations (Eq. 38) presented earlier. This allows us to include/omit particular geometric loss cases that occur/do not occur to improve computational speed. Depending on when the pass ends, different numbers of piecewise integrations are performed within which eclipses are also included. The procedure does not explicitly include the attitude of the reflector. The assumed circular shape of solar power farms enables us to omit specific azimuthal ori-

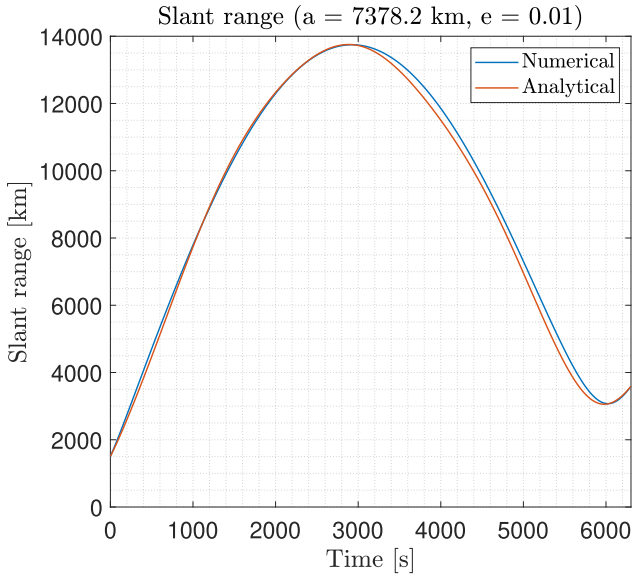

(a) $e = 0.01$

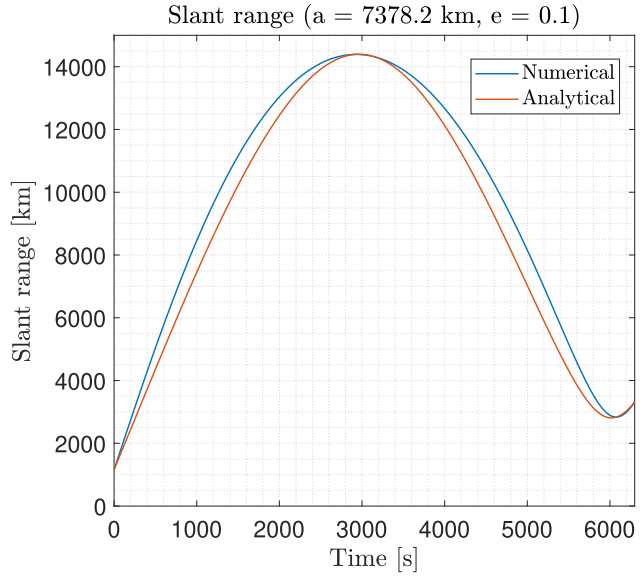

(b) $e = 0.1$

Fig. 11. The semi-analytically generated slant range for one orbit period of two elliptical orbits of the eccentricity of 0.01 (left) and 0.1 (right).

entations of the solar image. The computational speed of the code for reference case that has been considered throughout the paper (SSO of 1000 km altitude) is typically between 0.1 to 0.13 s on a typical laptop computer.

4.6.2. Model applicability for elliptical orbits

The model can in principle be expanded into elliptical orbits, as the geometry of the solar image can be generalised. However, the dynamical aspects of the energy delivery model are not as straightforward as it is for circular orbits. The current implementation relies on linear propagation of all time-dependent parameters for their simplicity and computational speed, without compromising the model's accuracy and sophistication. Satisfying these demands for elliptical orbits is challenging without a compromise in any of these aspects. For instance, integrating Eq. (26) over time means solving Kepler's equation numerically. If instead Eq. (26) is expressed in terms of true anomaly, then parameters such as the Earth rotation also need to be expressed in units of true anomaly. The low-order description of the Earth's oblateness also becomes a challenge, especially when the orbit eccentricity is increased. Fig. 11 below shows two examples of the slant range for one orbital period, as calculated for two elliptical orbits with eccentricities of 0.01 and 0.1.

In Fig. 11, the slant range is expressed analytically in terms of true anomaly, except for the Earth's rotation, which is expressed as a function of time, found from the true anomaly. The numerical simulation is performed with a J_2-enhanced two-body propagator, and appropriate transformations are made to obtain the slant range from the simulation output. The results show that, even for a nearly circular orbit at $e = 0.01$, the error between the numerical and analytical results builds up rapidly. For the results in the left panel, the error is within 10%. Note that the error is 0.3% at a maximum for circular orbits. When the eccentricity is increased to 0.1 the error grows to more than 15%. It was found that the low-order description of the Earth's oblateness is the likely cause of the discrepancy. It appears that Eqs. (13) and (14) cannot accurately capture the short-period variations in the orbital elements due to the Earth's oblateness, even though they appear to capture the average dynamics over an orbit period. However, these short-period variations are important as the slant range is calculated within a portion of the orbit. Including higher-order terms of the Earth's oblateness would improve the accuracy. However, this was not included in the current paper to retain a level of simplicity and computational speed. Nevertheless, the model described throughout the paper may still be useful for mildly elliptical orbits ($e < 0.01$) and/or for high-altitude orbits where the effect of the Earth's oblateness is smaller. On the other hand, at lower altitudes where the effect of the Earth's oblateness increases, the eccentricity range may be further limited.

5. Applications

5.1. Solar energy delivery from (near-) polar orbits

The delivery of reflected solar energy from a polar orbit will be investigated first, as it provides a test bed to compare the results of the model presented in this paper against the previous works on the subject by Fraas (2012) and Çelik and McInnes (2022). Both of these works considered a 1000 km polar orbit and non-rotating Earth. Even with this model, by including geometric losses (as discussed in Section 4.3) and atmospheric losses more accurately, Çelik and McInnes (2022) demonstrated that previous

works overestimate the quantity of energy delivery by more than fourfold (Çelik and McInnes, 2022). This paper presents a model that is higher fidelity than both of the previous works and includes effects such as the Earth's rotation, which makes a direct comparison challenging. This will still be attempted by finding a near-overhead pass over an equatorial solar power farm for a 1000 km polar orbit, placed at the terminator line ($\Omega = 90$ deg). It was found that this occurs approximately $\lambda_o = 88$ deg, hence this value will be used as the initial solar power farm position. The solar power farm is a circular disk with a diameter of 10 km and the reflector has a 1 km diameter. Note in this case that, due to the polar orbit choice, the Earth's oblateness will not affect the results. The power profile of this pass is presented in Fig. 12.

The duration for this pass is 1054.22 s, approximately 3 s shorter than the pass duration for a non-rotating solar power farm (Çelik and McInnes, 2022), which confirms the near-overhead pass. When non-rotating Earth is considered, the power profile is symmetric, provided that there is no panel tilt considered, as in the case here. When all geometric cases occur as discussed in Section 3, the profile starts with a solar image larger than the solar power farm and follows a brief period where the solar image semi-minor axis (b) is smaller than the solar power farm radius (R_{gt}), before the solar image is fully contained within the solar power farm boundaries. This last phase is where the peak power occurs due to the smaller solar image, generally at the zenith point of the pass. However, in the case here, despite the similarity in the pass duration, the inclusion of the Earth's rotation appears to distort the otherwise symmetric profile in Çelik and McInnes (2022). All geometric phases still occur, but the highest power delivery skews towards the first half of the pass, shortly before the halfway point. The power delivered decreases beyond this point. When the geometric case 3 (red dots) occurs in the second half of the pass after around $t = 550$ sec, the power value is generally lower than the same phase in the first half of the pass, which suggests a more stretched image (larger a and b) at this phase than in the first half. This may be expected as in the first half of the pass the reflector and the solar power farm are approaching each other, while in the second half, they move away. The quantity of energy delivered is found to be 35.06 MWh in this case. Table 3 presents a comparison between this result and the other works.

In a recently published work, Fraas and O'Neill (2023) presented their results for the quantity of energy delivered for a 1-km reflector in a 1000-km altitude polar orbit. The authors implement a geometric analysis to calculate a power profile similar to this work. Although not explicitly stated in Fraas and O'Neill (2023), the authors of this paper believe that their calculation also includes atmospheric transmission losses as the quantity of energy delivered found in Fraas and O'Neill (2023) is equal to 38 MWh, very close to the results of Çelik and McInnes (2022) and this paper. The reason for the small discrepancy

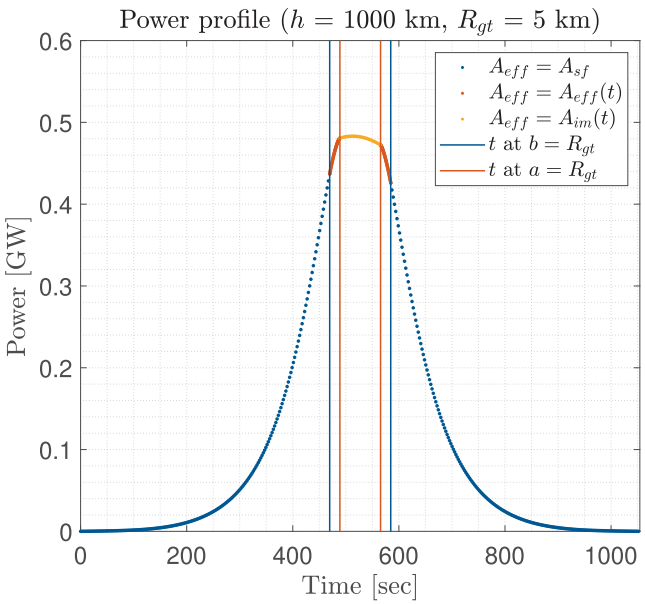

Fig. 12. The power profile of the solar energy reflected to a 10 km diameter solar power farm by a 1 km diameter reflector from a 1000 km altitude polar orbit.

between Fraas and O'Neill (2023), Çelik and McInnes (2022) and this paper is not clear, but it may be due to the larger integration step size that appears to be chosen in Fraas and O'Neill (2023). Nevertheless, the similarity between the works provides an independent validation of the results in this paper. On the other hand, the contrast between the results of this work and Çelik and McInnes (2022) is more subtle. The decrease in energy delivered by the inclusion of the Earth's rotation is approximately 0.14 MWh. One might argue that the complexity of the modelling in this paper may not be justified by the improvement obtained in the results. However, the previous work by Çelik and McInnes (2022) could only be applied to the polar orbits, while the model in this paper can in principle be expanded to any circular orbit and particularly to Sun-synchronous orbits, which are more relevant for orbiting solar reflector applications. Sun-synchronous orbits are one of the prime candidate orbits for orbiting solar reflector applications (Viale et al., 2023), as the orbit plane can be normal to the Sun-line as the Earth orbits the Sun through nodal precession thanks to the Earth's oblateness and can be eclipse-free for most of the year. Utilising the Earth's oblateness requires SSOs to be in a certain inclination for a given altitude (Chobotov, 2002). For low-Earth orbit altitudes, this is close to 90deg but significantly deviates from it as the orbit altitude increases, which requires the higher fidelity modelling that is presented in this paper.

An analysis will now be presented for the example Sun-synchronous orbit used throughout the paper to demonstrate the capabilities of the modelling of reflected solar energy delivery. This orbit is a 1000 km altitude circular orbit and placed at the terminator line ($\Omega = 90$ deg), which

Table 3
A comparison of the quantity of the energy delivered between Fraas and O'Neill (2023), Çelik and McInnes (2022) and this study for a 1 km diameter reflector at a 1000 km polar orbit

Study	Losses	Delivered energy during a pass [MWh]
Fraas and O'Neill (2023)	Atmospheric losses, Geometric losses	38
Çelik and McInnes (2022)	Atmospheric transmission, Geometric losses	35.20
This paper	Atmospheric transmission, Geometric losses, Earth's rotation	35.06

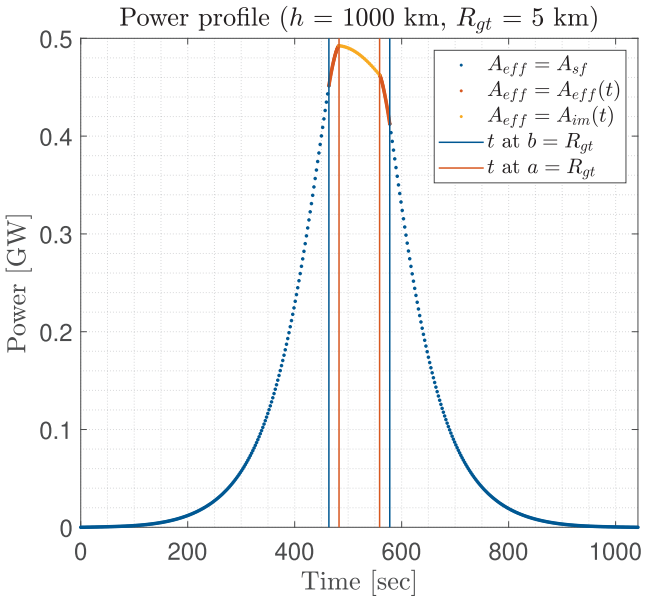

Fig. 13. The power profile of the solar energy reflected to a 10 km diameter solar power farm by a 1 km diameter reflector from a 1000 km altitude Sun-synchronous orbit.

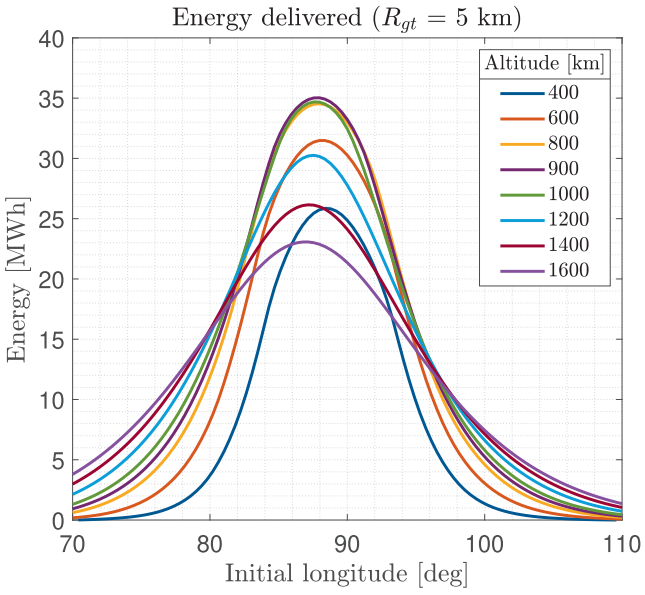

Fig. 14. The quantity of energy delivered by a 1 km diameter reflector from different altitudes of Sun-synchronous orbits.

can also be used to draw comparisons with the simple polar orbits presented in the previous subsection. The orbit inclination can be calculated as $i = 99.48$ deg. As can be seen, this is nearly a polar orbit, hence the final results may not be substantially different from the polar orbit case, especially if a near-overhead pass is selected, but this does not discount the fact that the model at hand is applicable to a much wider variety of cases. Again, a near-overhead pass is selected with $\lambda_o = 88$ deg for an equatorial solar power farm ($\phi = 0$ deg). This results in an initial argument of latitude of the pass being $\theta_o = -29.79$ deg and a pass duration $T_{pass} = 1041.8sec$ by using the techniques described in the previous sections. According to these initial conditions, the profile of the power delivered is presented in Fig. 13.

The profile in Fig. 13 is more skewed compared to its polar orbit counterpart in Fig. 12. All three geometric cases appear in the profile. However, the highest quantity of power is delivered around the transition point between cases 2 and 3 (yellow and red points, respectively). The solar power farm and the reflector are approaching each other in the first half of the pass, but this time, due to the orbit inclination, the maximum power delivery is skewed towards an earlier time than a simple polar orbit. The profile becomes sharper as the reflector and the solar power farm move in opposite directions much faster due to the orbit inclination. Note the orbit inclination here also relates to the nodal precession which affects both the right ascension of the ascending node and the argument of latitude.

The quantity of energy delivered is equal to 34.7 MWh. This value is close to but smaller than the polar orbit cases considered in the previous subsection. The decrease in energy delivered may not appear substantial, but it can make a considerable impact on daily energy delivery when multiple passes are considered. A possibly important point to note is that the maximum quantity of power delivered is higher in the Sun-synchronous orbit than in the polar orbit, but the area under the curve is smaller. This highlights that sampling a single value of power profile and extrapolating it for the quantity of energy may not be representative of the total quantity of energy, again highlighting the high-fidelity approach taken here.

Throughout this paper, a 1000 km orbit is considered as an example. Now, the analysis will be extended to different orbit altitudes of SSOs and different λ_o values. The SSO inclinations are calculated for altitudes between 400 km and 1600 km and λ_o values between 70 deg and 110 deg. The pass duration and other related parameters are

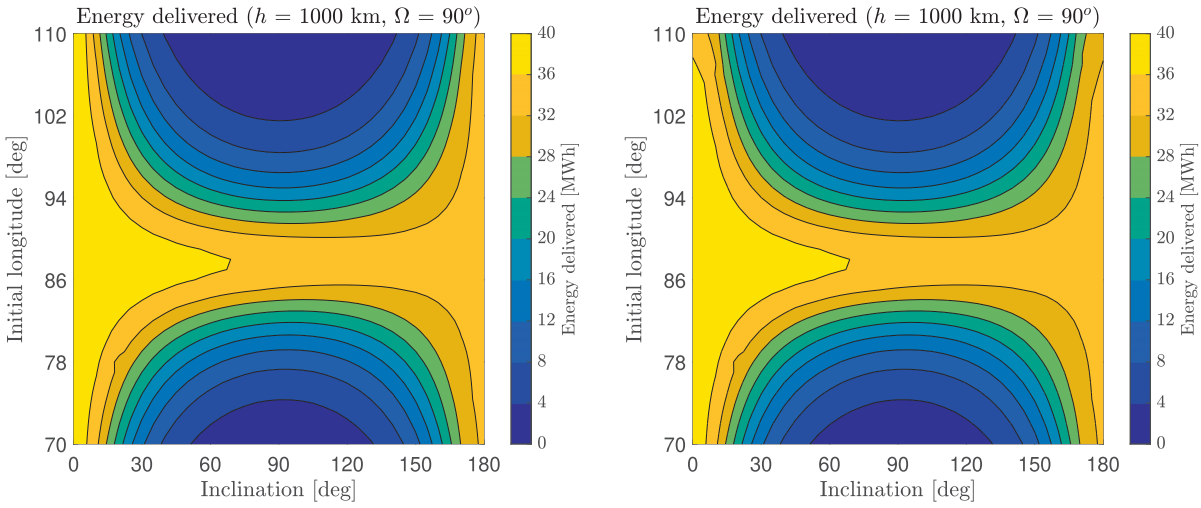

(a) No eclipse (b) Eclipses included

Fig. 15. The quantity of energy delivered by a 1 km diameter equivalent reflector from a Sun-synchronous orbit of 1000 km altitude, for a range of equatorial solar power farm longitudes. Solar power farm diameter is 10 km.

calculated according to the methodology presented in the earlier sections. The results are presented in Fig. 14.

Among the orbit altitudes considered, the range between 800 and 1000 km appears to be the optimum range, within which 900 km appears to be the optimum altitude for the maximum quantity of energy delivered. For all three altitudes, the maximum quantity is approximately 35 MWh and can be delivered for $\lambda_o \approx 88$ deg. There are then high and low altitude pairs outside this optimum range, such as 600 km and 1200 km and 400 km and 1400 km where the maximum energy delivery is similar. Low altitude orbits provide short passes but higher solar energy density. The opposite is the case for higher altitude orbits. Generally, the similarity is due to the compensation of short passes with higher power density in lower altitude orbits and lower power density with longer passes in higher altitude orbits. However, the appearance of Fig. 14 can be different if the solar power farm size is different. For example, in a hypothetical case of a projected solar image contained within the solar power farm boundaries (geometric loss case 2 in Section 4.3) throughout the pass, the quantity of energy delivered would be the highest for the highest altitude instead, as the pass duration is the highest and the effective solar power farm area is equal to the area of the solar image. However, one should also note the impact of the orbit inclination as it changes for different altitudes for Sun-synchronous orbits. Another potentially interesting result is for 1600 km altitude, the highest considered, where the quantity of the energy delivered is the highest at the extremes of the λ_o range due to the longest pass duration. Related to this point, the quantity of energy delivered is generally less at the extreme points at the night side longitudes than that of the day side due to the eclipses implemented in this model.

5.2. Effects of orbit inclination and non-equatorial solar power farms

To demonstrate further advantages of the model in this paper, the analysis will be extended to other orbit inclinations between 0 deg and 180 deg, and λ_o between 70 deg and 110 deg for equatorial solar power farms. This analysis also relates to the discussion on eclipses, as the reflectors at some of the low inclination orbits will be eclipsed during the energy delivery to the night-time longitudes. This will be demonstrated with a hypothetical no-eclipse energy delivery case, as shown in Fig. 15.

New insights into the solar energy delivery problem can be obtained from this analysis. First of all, the quantity of energy delivered can be higher than approximately 35 MWh presented in this paper and in Çelik and McInnes (2022). The maximum value is approximately 38 MWh and these higher values appear at equatorial inclinations for most λ_o values and in a narrower band of λ_o values for inclinations up to 75deg. These can be explained by the direction of the motion of the reflector, which maximises the pass duration for equatorial longitudes, as the orbital motion is prograde, which also appears to be effective for a band of longitudes at higher orbit inclinations. Retrograde equatorial orbits also deliver energy at similar levels as near-polar orbits as the pass geometry is favourable, despite the shortened pass duration. The quantity of energy delivered varies the most for near-polar orbits, which is extremely low at large and small λ_o values and maximised at $\lambda_o = 90$ deg as discussed throughout. The right panel of Fig. 15 shows the decrease in the quantity due to the inclusion of eclipses. Despite the shortened total pass duration due to eclipses (as shown in Fig. 9), the decrease in the quantity of energy delivered appears to be

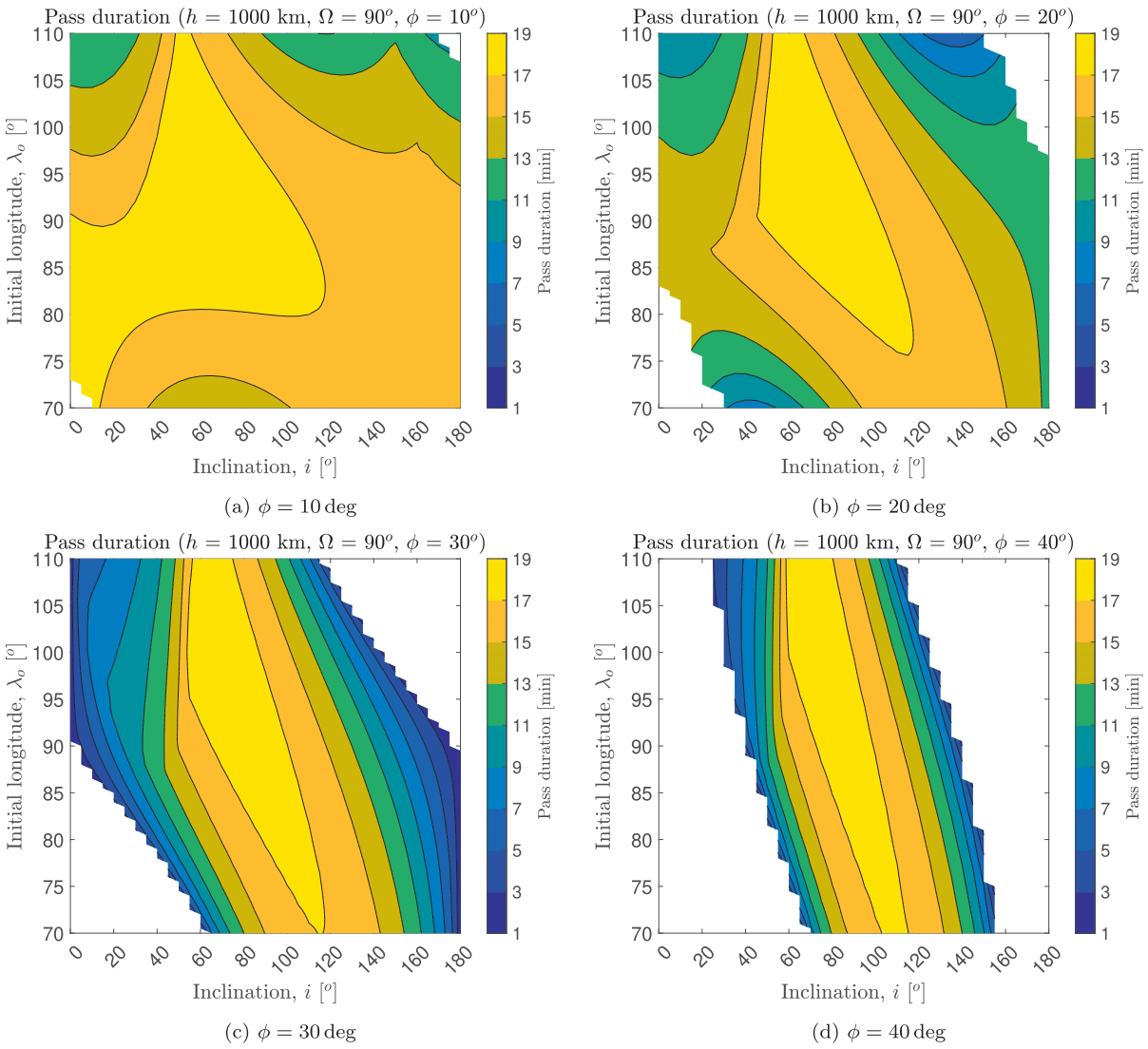

(a) $\phi = 10$ deg (b) $\phi = 20$ deg

(c) $\phi = 30$ deg (d) $\phi = 40$ deg

Fig. 16. Pass duration for a 1000 km altitude Sun-synchronous orbit at different inclinations and non-equatorial solar power farms, with eclipses included.

relatively modest. Power profiles in Figs. 12 and 13 show that the majority of the energy is delivered in the middle portion of a pass, for approximately 300 sec. Eclipses outside of this zone do not affect the final quantity of energy delivered substantially, as the results show in Fig. 15.

Thus far the analyses are considered for the case of equatorial solar power farms, but the majority of existing and planned solar power farms are in non-equatorial latitudes as high as approximately 40 deg latitude Viale et al. (2023). The solar power farm latitude ϕ will then be increased to 10, 20, 30 and 40 deg respectively to analyse its effect on the quantity of energy delivered close to the Earth's terminator line. As considered throughout this paper, a 1000 km altitude circular orbit placed at the terminator line is considered. The inclination is varied between 0 and 180 deg and the initial solar power farm longitude between 70 and 110 deg. First, Fig. 16 shows how the pass duration evolves with the solar power farm latitude.

Note that eclipses are included in the calculation of the pass duration. The pass duration is between a few minutes and up to 19 min as shown in the previous analyses in the paper. From the top left to the lower right, the figures show fewer contact opportunities from low inclination orbits as ϕ increases. The orbit inclinations between 60 and 80 deg and night-time longitudes ($\lambda_o > 90$ deg) repeatedly provide the highest pass duration in all cases. The longer pass duration due to the prograde motion becomes limited to higher inclination orbits as ϕ increases. It can be expected that the contour map will be defined by straight vertical lines, i.e., fixed pass duration for all longitudes for a given inclination, at $\phi = 90$ deg, where different λ_o values correspond to the same pole point. In light of these results, Fig. 17 shows maps of the quantity of energy delivered for the same initial conditions.

In general, the availability of energy delivery becomes limited as ϕ increases. At the highest ϕ considered in this

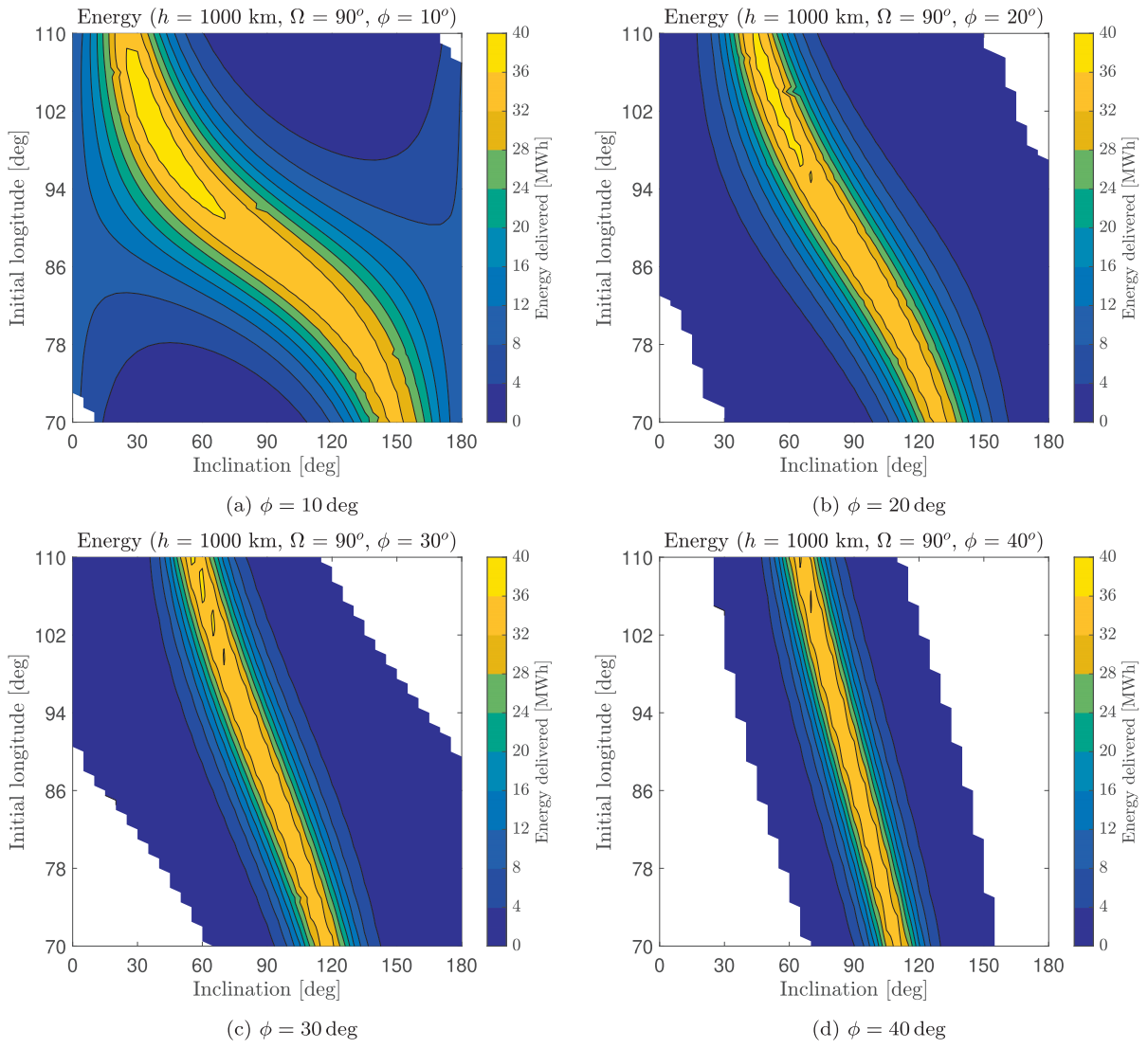

(a) $\phi = 10$ deg (b) $\phi = 20$ deg

(c) $\phi = 30$ deg (d) $\phi = 40$ deg

Fig. 17. The quantity of energy delivered by a 1 km diameter reflector from a 1000 km circular orbit at different inclinations and non-equatorial solar power farms. The solar power farm diameter is 10 km.

paper (lower right figure), energy delivery is only possible between inclinations 30 and 150 deg and for quantities of energy delivered up to 36 MWh, except for two small islands where it is greater than 36 MWh. Those islands are larger at lower ϕ values and between inclinations of 30 deg and approximately 85 deg and in nighttime longitudes. This is in line with the higher pass duration for prograde orbits around these inclinations and initial longitudes shown in Fig. 16. Due to the shrinking of the range of orbit inclinations with increasing ϕ, the quantity of energy delivered becomes closer to the cases where the Earth is non-rotating. As discussed for the pass duration case, for $\phi = 90$ deg, the model would effectively behave as if the Earth is non-rotating as the pole point does not rotate. At the pole point, the highest quantity of energy can only be delivered by a polar orbit. To that end, Çelik and McInnes (2022) finds that for a 1000 km polar orbit, the quantity of energy delivered is equal to 35.2 MWh (also shown in Table 3). The convergence of the highest quantity of energy delivered towards the range of 32–36 MWh then becomes in line with the results of Çelik and McInnes (2022). This consistency in energy delivery builds confidence in the sophisticated model presented in this paper to then consider it for a wider range of orbits and solar reflector applications. However, the sophistication of the model can be further demonstrated by analysing the seasonal energy delivery.

5.3. Seasonal variations

The final analysis will be made on seasonal variations. This analysis includes the Earth's obliquity and orbit around the Sun, which changes the direction of the effective Sun vector. The variation in the Sun vector direction induces small variations in the angle of incidence and also changes the direction of the Earth's shadow cone. How-

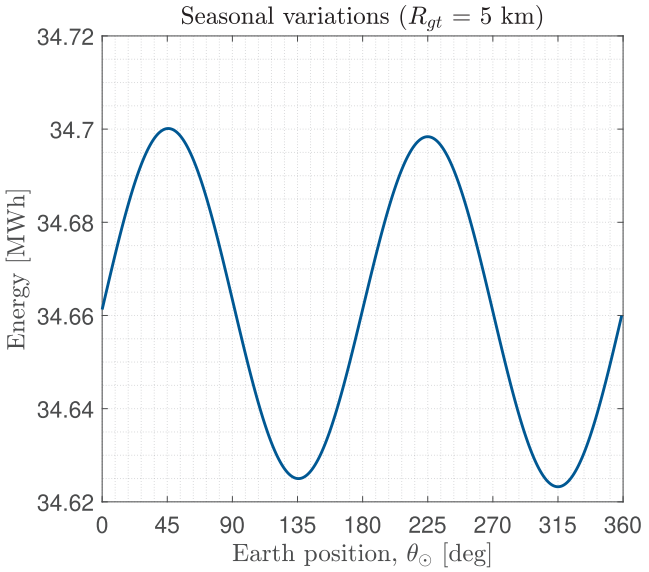

Fig. 18. Energy delivered at different positions of the Earth around the Sun.

ever, it is expected that the eclipses have minimal impact on the quantity of energy delivered from SSOs placed on the terminator line.

To demonstrate the variation in the quantity of energy delivered, again, an SSO at 1000 km altitude is considered. The orbit is placed at the terminator line and is assumed to deliver solar energy to an equatorial solar power farm of 10 km diameter. The local time, or the initial longitude, is $\lambda_o = 88$ deg. The Earth's position is expressed as the angle from the vernal equinox day, where $\theta_\odot = 0$ deg and increased by 1deg or approximately by a day. The results are presented in Fig. 18.

The results show minimal variation in the quantity of energy delivered. The difference between the maximum and minimum is approximately 70 kWh. The maximum quantity appears to be sometime between the vernal equinox and summer solstice. The maximum energy delivered between the autumn equinox and winter solstice is slightly smaller than this. Similarly, the minimum values of energy delivered are between the summer solstice and autumn equinox, and the winter solstice and vernal equinox. Again, the former is slightly greater than the latter. On average, the quantity of energy delivered is equal to 34.66 MWh throughout the year. This consistency in energy delivery builds confidence in the employment of orbiting solar reflectors for solar energy applications throughout the year.

6. Conclusion

The potential of orbiting solar reflectors can be assessed with high-fidelity modelling of the quantity of energy delivered to illuminate terrestrial solar power farms to enhance their utility beyond the hours of daylight. This paper has presented a high-fidelity, semi-analytical model to calculate the reflected solar energy from circular orbits. The model has been developed such that for a given input of orbital elements and initial solar power farm position from the Sun-line (i.e., local time), the output is the quantity of energy delivered. An idealised flat reflector and a circular solar power farm are assumed, but the model includes the Earth's oblateness, rotation and the Earth's orbit around the Sun and eclipses, in addition to time-dependent geometrical area relationships between the image of the solar disk and the solar power farm, and atmospheric losses. This extends the model to be applicable to circular orbits at different inclinations, and particularly to Sun-synchronous orbits that are relevant for space-based solar energy applications. The final integration is piecewise due to different geometrical relationships and can only be solved numerically. However, analytical insights are presented for variable pass durations, eclipses, angle of incidence and other geometrical relationships.

The results show that the Earth's rotation, the orbital elements, particularly the reflector orbit inclination, and eclipses affect the energy delivered depending on the initial solar power farm position. Prograde orbits generally provide higher energy delivery due to longer pass durations. However, the difference between prograde and retrograde orbits is reduced as the solar power farm latitude increases and disappears at the pole point. Indeed, a point at the pole will be stationary and the current model can be validated with our previous study where the Earth is assumed to be non-rotating. This validation also demonstrates that the current model is more general than existing models. Other applications show that for a range of Sun-synchronous orbit altitudes, 1 km diameter reflector and 10 km diameter circular solar power farm, the largest quantity of energy delivered would be between 800 and 1000 km altitudes.

The model presented in this paper offers insights into the reflected solar energy delivery problem that were not offered in previous papers. The results for the Earth can be used in the design of orbiting solar reflector missions that enhance the utility of terrestrial solar power in the realisation of a truly global clean energy service. The model can in principle be extended to other planetary bodies.

Declaration of competing interest

The authors declare that they have no known competing financial interests or personal relationships that could have appeared to influence the work reported in this paper.

Acknowledgments

This project has received funding from the European Research Council (ERC) under the European Union's Horizon 2020 research and innovation programme (grant agreement No. 883730). CRM is also supported by the Royal Academy of Engineering under the Chair in Emerging Technologies scheme.

Appendix A. Rotation matrices

The successive rotations about an axis j ($j = 1,2,3$) can be expressed by using Euler angles and three rotation matrices as follows (Schaub and Junkins, 2009):

$$M_1(v_1) = \begin{bmatrix} 1 & 0 & 0 \\ 0 & \cos v_1 & \sin v_1 \\ 0 & -\sin v_1 & \cos v_1 \end{bmatrix} \tag{A.1a}$$

$$M_2(v_2) = \begin{bmatrix} \cos v_2 & 0 & -\sin v_2 \\ 0 & 1 & 0 \\ \sin v_2 & 0 & \cos v_2 \end{bmatrix} \tag{A.1b}$$

$$M_3(v_3) = \begin{bmatrix} \cos v_3 & \sin v_3 & 0 \\ -\sin v_3 & \cos v_3 & 0 \\ 0 & 0 & 1 \end{bmatrix} \tag{A.1c}$$

A rotation matrix sequence, such as 3-1-3 used in this paper, can be created such that:

$$M_{313} = M_3(v_3)M_1(v_1)M_3(v_3) \tag{A.1}$$

where v_j denotes the angle of rotation, e.g. an orbital element.

Appendix B. Calculation of shadow cones

The calculation procedure in this section is a summary of the discussion in Longo and Rickman (1995). The angles and lengths used in these calculations are presented in Fig. B.1.

In the case of the umbra cone, its height can be found as follows:

$$\rho_u = \frac{R_E \rho_{sun}}{R_{sun} - R_E} \tag{B.1}$$

and the apex angle α_u can be found by using trigonometry:

$$\alpha_u = \arcsin \frac{R_E}{2\rho_u} \tag{B.2}$$

Similarly the penumbra cone can be determined by first finding the distance ρ_p:

$$\rho_p = \frac{R_E \rho_{sun}}{R_{sun} + R_E} \tag{B.3}$$

Again, the apex angle α_p can be from trigonometry:

$$\alpha_p = \arcsin \frac{R_E}{2\rho_p} \tag{B.4}$$

The entry point of the umbra cone is then found by using both the cone height ρ_u and its half angle α_u, and the projected position of the reflector on the Sun line (see Section 4.2 and Fig. 7 for details), such that:

$$\xi_u = (\rho_u - \| \mathbf{X}_{pr} \|) \tan \alpha_u \tag{B.5}$$

Similarly, the entry point of the penumbra cone can be found using ρ_p, α_p and $\vec{X}_{pr}$:

$$\xi_p = (\rho_p + \| \mathbf{X}_{pr} \|) \tan \alpha_p \tag{B.6}$$

Then, by subtracting the reflector's projected position on the Sun line from its orbital position, the vector perpendicular to the Sun line ($\delta(t)$ in Section 4.2) can be found. If the magnitude of this vector is smaller than ξ_u and ξ_p, then the reflector is in penumbra or umbra, respectively. The points where $\delta(t)$ is equal to ξ_u or ξ_p would indicate the beginning or end of the penumbra or umbra eclipse duration, which are used in this paper to determine the eclipse period of the reflector's pass over a solar power farm.

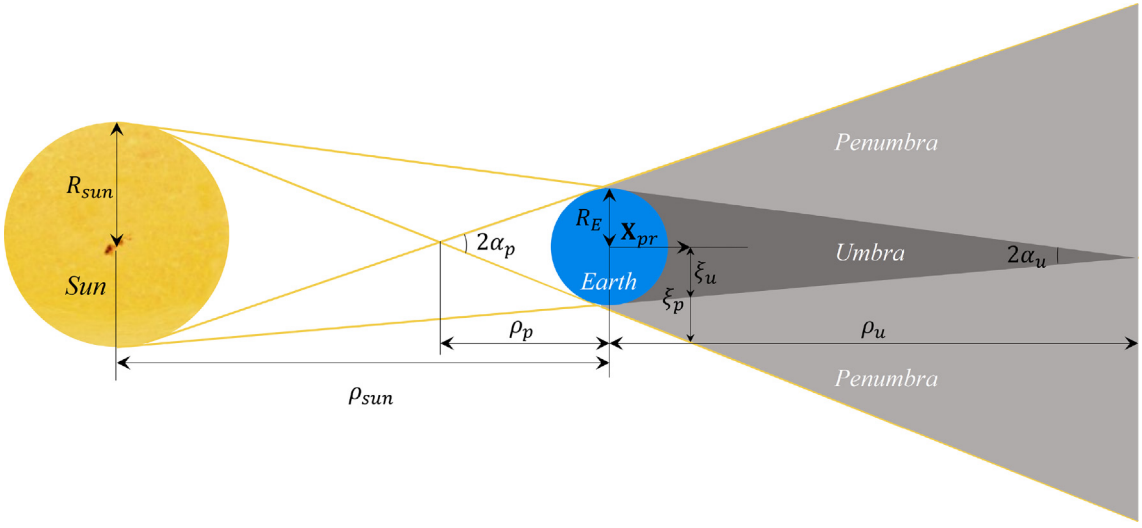

Fig. B.1. Eclipse geometry and different parameters used in the calculations.

References

Bewick, R., Sanchez, J.P., McInnes, C.R., 2011. Use of orbiting reflectors to decrease the technological challenges of surviving the lunar night. In: 62nd International Astronautical Congress (IAC 2011). Cape Town, South Africa: IAF volume 2. Paper no. IAC-11-A5.1.11, pp. 1597–1609.

Billman, K.W., Gilbreath, W.P., Bowen, S.W., 1977. Introductory assessment of orbiting reflections for terrestrial power generation. Technical Report NASA-TM-73230 NASA.

Bonetti, F., McInnes, C., 2019. Space-enhanced terrestrial solar power for equatorial regions. J. Spacecraft Rock. 56, 33–43.

Buckingham, A.G., Watson, H.M., 1968. Basic concepts of orbiting reflectors. J. Spacecraft Rock. 5, 851–854.

Canady, J.E., Allen, J.L., 1982. Illumination from space with orbiting solar-reflector spacecraft. Technical Report NASA-TP-2065 NASA.

Çelik, O., McInnes, C.R., 2023. A constellation design for orbiting solar reflectors to enhance terrestrial solar energy. In: 74th International Astronautical Congress (IAC 2023). Baku, Azerbaijan: IAF. Paper no. IAC-23-C1,IPB,4,x77299.

Çelik, O., Viale, A., Oderinwale, T., Sulbhewar, L., McInnes, C.R., 2022. Enhancing terrestrial solar power using orbiting solar reflectors. Acta Astronaut. 195, 276–286.

Çelik, O., McInnes, C.R., 2022. An analytical model for solar energy reflected from space with selected applications. Adv. Space Res. 69, 647–663.

Chobotov, V.A., 2002. Orbital Mechanics. AIAA.

Curtis, H., 2013. Orbital Mechanics for Engineering Students. Butterworth-Heinemann.

Ehnberg, J.S., Bollen, M.H., 2005. Simulation of global solar radiation based on cloud observations. Sol. Energy 78, 157–162.

Ehricke, K.A., 1979. Space light: space industrial enhancement of the solar option. Acta Astronaut. 6, 1515–1633.

Forsythe, G.E., Malcolm, M.A., Moler, C.B., 1977. Computer Methods for Mathematical Computations, vol. 259. Prentice-Hall Inc..

Fraas, L.M., 2012. Mirrors in space for low-cost terrestrial solar electric power at night. In: 38th IEEE Photovoltaic Specialists Conference. IEEE, Austin, TX, pp. 2862–2867.

Fraas, L.M., Landis, G.A., Palisoc, A., 2013. Mirror satellites in polar orbit beaming sunlight to terrestrial solar fields at dawn and dusk. In: 2013 IEEE 39th Photovoltaic Specialists Conference (PVSC). IEEE, Tampa, FL, pp. 2764–2769.

Fraas, L.M., O'Neill, M.J., 2023. Sunbeams from space mirrors for terrestrial pv. In: Low-Cost Solar Electric Power. Springer International Publishing, Cham, pp. 163–176.

Giorgini, J.D., 2015Status of the JPL horizons ephemeris system. In: IAU General Assembly. vol. 29.

Hottel, H.C., 1976. A simple model for estimating the transmittance of direct solar radiation through clear atmospheres. Sol. Energy 18, 129–134.

Çelik, O., McInnes, C.R., 2022. Families of displaced non-keplerian polar orbits for space-based solar energy applications. In: 73rd International Astronautical Congress (IAC 2022). Paris, France: IAF. Paper no. IAC-22-C1.IP.37.x69012.

Oberth, H., 1929. Methods of space travel. Munich, Oldenburg, p. 494.

Ortiz Longo, C.R., Rickman, S.L., 1995. Method for the calculation of spacecraft umbra and penumbra shadow terminator points. Technical Report NASA-TP-3547.

Schaub, H., Junkins, J.L., 2009. Analytical Mechanics of Space Systems. American Institute of Aeronautics and Astronautics.

Viale, A., Çelik, O., Oderinwale, T., Sulbhewar, L., Bailet, G., McInnes, C.R., 2022. Towards the commercial development of orbiting reflectors: a technology demonstration roadmap. In: 73rd International Astronautical Congress (IAC 2022). Paris, France: IAF. Paper no. IAC-22-C3.2.x70070.

Viale, A., Çelik, O., Oderinwale, T., Sulbhewar, L., McInnes, C.R., 2023. A reference architecture for orbiting solar reflectors to enhance terrestrial solar power plant output. Adv. Space Res. 72, 1304–1348.